Pergamon

Geochimica et Cosmochimica Acta, Vol. 65, No. 9, pp. 1399–1416, 2001

0016-7037/01 $20.00 + .00

PII S0016-7037(01)00552-X

Variations in pyrite texture, sulfur isotope composition, and iron systematics in the Black Sea: Evidence for Late Pleistocene to Holocene excursions of the O_2-H_2S redox transition

RICHARD T. WILKIN[†,*] and MICHAEL A. ARTHUR

Department of Geosciences and Penn State Astrobiology Research Center, Pennsylvania State University, University Park, PA 16802, USA

(*Received May* 1, 2000; *accepted in revised form December* 20, 2000)

Abstract—Time-dependent variations in the physicochemical properties of pyrite were investigated in four sediment cores from the Black Sea. In the laminated, deep-basin sediments of Unit I and Unit II, >86% of pyrite particles are present as fine-grained framboidal aggregates. In these sediments, the dominance of pyrite framboids, with a narrow size distribution and maximum size < 18 μm, is evidence of syngenetic (water column) pyrite formation subjacent to the O_2-H_2S boundary. Sediments from the basin margin collected below the impingement of the O_2-H_2S boundary contain an increased proportion of fine-grained euhedral grains of pyrite relative to framboidal aggregates, suggesting increased additions of diagenetic pyrite below the sediment-water interface. The more efficient reduction and sulfidation of iron in the water column of the central region of the basin implies a more reactive source of iron there compared to the basin margins, and is tied to increasing %pyrite as framboids and greater degrees of pyritization (DOP) in the basin center relative to the basin margins. An evaluation of Fe-S-C relations indicates that pyrite formation was limited by sulfate availability during deposition of the oldest lacustrine sediments of Unit III, C-limited for upper Unit III due to the input of sulfate-rich Mediterranean seawater, and Fe-limited in the laminated, organic carbon-rich sediments of Units I and II. These changes in pyrite-limiting factors occurred within 4 m of compacted burial representing <15 ka. Sediment fabric and framboid size distributions at a shallow, basin-margin site suggest that during two extended periods of Unit II deposition, the O_2-H_2S transition retreated to depths below 200 m. However, during these same intervals, the $\delta^{34}S$ of pyrite remains uniform compared to overlying and underlying laminated sediments, implying that this chemical signature may not be uniquely tied to the position of the O_2-H_2S boundary relative to the sediment-water interface, but rather is likely related to biogeochemical processes.

1. INTRODUCTION

The Black Sea basin is often regarded as a modern analog for Precambrian and Phanerozoic environments where thick sequences of marine black shales were deposited (e.g., Degens and Stoffers, 1976; Arthur and Sageman, 1994). Such uniformitarian comparisons stem from the fact that the Black Sea contains a large volume of deep, anoxic, and sulfidic water with underlying sediments that are finely laminated and rich in organic carbon. Despite the common application of the Black Sea as a type example of an anoxic basin, uncertainty remains about the details of the temporal and chemical evolution of the deep anoxic water and its imprint on the physical and chemical properties of sediment in the Black Sea. For example, with respect to the early Holocene history there is controversy between investigators favoring high biologic productivity coupled with an oxygenated water column and those favoring long-term water column anoxia as the primary controls on deposition of organic carbon-rich sediments in the Black Sea and black shales in general (Calvert, 1990; Pedersen and Calvert, 1990; Arthur and Dean, 1998). A common goal in sedimentary geochemistry, therefore, is the identification of robust inorganic and organic proxies that record water column chemistry, especially water column oxidation states. The Black Sea represents a key modern environment in which proposed methodologies can be tested for evaluating ancient depositional environments and oceanic redox chemistry.

The physical and chemical properties of sedimentary pyrite provide important records of the ocean's response to changing environmental conditions in the past and linkages to the global geochemical cycles of iron, sulfur, carbon, and oxygen. Developing an understanding of the processes that control these properties of sedimentary pyrite is, therefore, a fundamental goal of marine geochemistry. Moreover, iron sulfide formation in sedimentary environments is a prime example of a mineral crystallization mechanism governed by the oftentimes poorly understood interactions between biotic and abiotic processes. In these contexts, the study of the physicochemical properties of pyrite should contribute insights into the character and biogeochemical processes of ancient depositional environments and thereby constrain the exogenic cycle of ancient sedimentary systems.

Depth-dependent variations in the concentration of pyrite in a sediment column are typically interpreted as reflecting variations in the availability of organic carbon, iron, or sulfate (Berner, 1984). Field and experimental studies suggest that a fourth factor, oxidation rate, may also influence short-term (<100 yr) accumulation of FeS_2 (Gagnon et al., 1995; Wilkin and Barnes, 1997a; Hurtgen et al., 1999). The S isotopic composition of sedimentary sulfides reveals information about the role of sulfate-reducing bacteria and, possibly, the role of sulfide-oxidizing bacteria in forming aqueous sulfur species that precipitate as iron monosulfides and ultimately, as iron

*Author to whom correspondence should be addressed (wilkin.rick@epa.gov).
[†]*Present address:* National Risk Management Research Laboratory, U.S. Environmental Protection Agency, Ada, OK 74820, USA.

disulfides. Time-dependent changes in the sulfur isotope ratios of sedimentary pyrite may record changes in sulfate sources, changes in microbial communities and rates of microbial activity, or may reflect closed-system Raleigh isotope effects linked to basin hydrography and/or sedimentation rate.

Iron partitioning in sediments has been correlated with sedimentary depositional redox chemistry, in particular the ratio of sulfidized iron to other potentially reducible iron fractions (Canfield et al., 1996). Observations from both modern and ancient settings suggest that in many cases, the highest extents of Fe-mineral sulfidation are found in euxinic basins with bottom waters containing hydrogen sulfide (Raiswell et al., 1988; Lyons and Berner, 1992). Finally, textural properties of sedimentary pyrite provide information about the mechanisms of pyrite precipitation and can be used to evaluate the relative timing and location of pyrite formation in the sediment and water column (Raiswell, 1982; Wilkin et al., 1996; Passier et al., 1997). The extent to which nucleation or growth dominates the formation of pyrite can be directly assessed by an evaluation of pyrite morphology and particle size distribution. It is the goal of this study to present an integrated evaluation of sediment geochemical and physicochemical properties of pyrite in late Pleistocene to Holocene Black Sea sediments with the objective of testing and refining models for the development and evolution of the anoxic water mass over the past 15 ka, and to establish the potential of these techniques for application to the interpretation of redox histories of ancient oceans.

2. BACKGROUND

2.1. Black Sea Sedimentology

The Black Sea is a tectonically isolated basin. The Bosporus Strait, the Straits of the Dardanelles, and the Sea of Marmara provide a shallow connection between the Black Sea and the saline waters of the Aegean and Mediterranean seas. A permanent halocline at a depth of ~80 m in the center of the basin coincides with the redoxcline and separates the fresher, oxic surface waters from more saline, anoxic, and sulfidic deep waters. The hydrochemical structure of the Black Sea depends critically on freshwater inputs from rivers, atmospheric forcing, topography, and seawater inputs through the Bosporus (e.g., Özsoy and Ünlüata, 1997). During the last glacial maximum, seawater inputs from the Mediterranean were cut off, and the Black Sea was apparently a fully enclosed freshwater lake. As sea level rose, seawater entered the Black Sea system, either as a trickle (Degens and Ross, 1972), a catastrophic event (Ryan et al., 1997), or some combination of these two end-member scenarios (Arthur and Dean, 1998). At some point after the initial influx of seawater to the basin, water column anoxia developed. The geochemical and sedimentologic features of Black Sea sediments should provide evidence of this major oceanographic redox event and insight as to whether it occurred gradually or abruptly.

The principal features of the Black Sea sediments are described in Ross and Degens (1974), Hay et al. (1991), and Arthur et al. (1994), and most recently by Arthur and Dean (1998). The uppermost meter of sediment from the deep basin and basin margin contains up to four characteristic units. The most recent sediments (Unit I) consist of up to 55 cm of finely laminated, coccolith-bearing marl, which contains 1 to 5% organic carbon and 10 to 75% $CaCO_3$ (Arthur et al., 1994; Arthur and Dean, 1998). Below Unit I is an approximately 50-cm thick (up to 150 cm), finely laminated, carbonate-poor sapropel (Unit II), which contains 1 to 20% organic carbon and 5 to 15% $CaCO_3$. Homogeneous muds (turbidites) of variable thickness are commonly found interbedded with Units I and II in the deep portion of the basin but are less common on the basin slopes (e.g., Lyons, 1991). Estimates of the timing of the Unit I–II boundary range from 1.63 ka, based on varve counts (Hay et al., 1991; Arthur et al., 1994), to 2.7 ka based on bulk radiocarbon analyses of carbonate or organic carbon from samples collected from the deep basin (Jones and Gagnon, 1994). The upward transition from Unit II to Unit I marks the first appearance of *Emiliania huxleyi*, a coccolihophorid, which apparently indicates an increase in surface water salinity during Unit I deposition. The older Pleistocene-Holocene sediments, Unit III, are composed of massive to macrobanded, organic carbon-poor clays (<1% organic carbon). The age of the Unit II–III boundary is ~7.9 ka based on radiocarbon analyses (Jones and Gagnon 1984). This transition between Units II and III is marked by an upward increase in organic carbon content, from <1 wt.% in Unit III to the organic carbon-rich sapropels of Unit II, and a change from macroturbated clays (Unit III) to laminated sediments (Unit II) (Arthur and Dean 1998). Taken together, these units record the transition within the Black Sea from an oxic Pleistocene freshwater lake to the present anoxic-sulfidic marine basin.

Deuser (1974) suggested that oxygen depletion in the Black Sea water column began at ~9 ka, immediately after Mediterranean waters began spilling into the basin through the Bosporus Strait. The influx of saline waters led to density stratification in the basin, progressive depletion of deep water oxygen, and the slow, upward advance through the water column of the O_2-H_2S interface (see Glenn and Arthur, 1985; Degens et al., 1980). Based on radiocarbon dating (Jones and Gagnon 1994), varve counting, and sediment geochemical studies, Arthur and Dean (1998) proposed that the onset of water column anoxia was virtually synchronous at ~7.5 ka across the basin at depths below ~200 m. Furthermore, it appears that the position of the oxic-anoxic interface in the water column has been largely stationary over the past ~7.5 ka with the exceptions of possible short-term advances and retreats (e.g., Glenn and Arthur, 1985; Murray et al., 1989; Lyons et al., 1993; Sinninghe Damsté et al., 1993; Arthur and Dean, 1998). These changes in the depth of the chemocline are important because they could alter the spatial relationship between the oxic-anoxic boundary and the photic zone, thus affecting the organic geochemical character of the underlying sediments. In the sediments, the transition to anoxia is marked apparently by the Unit III to Unit II transition or the point where the sediments become both laminated and enriched in organic carbon (Wilkin et al., 1997; Arthur and Dean, 1998).

2.2. Pyrite Formation

Black Sea sediments have been the focus of numerous studies, which have been successful in illuminating the factors governing pyrite formation (e.g., Vinogradov et al., 1962; Berner, 1974; Calvert and Karlin, 1991; Lyons and Berner, 1992; Calvert et al., 1996; Lyons, 1997; Wilkin et al., 1997).

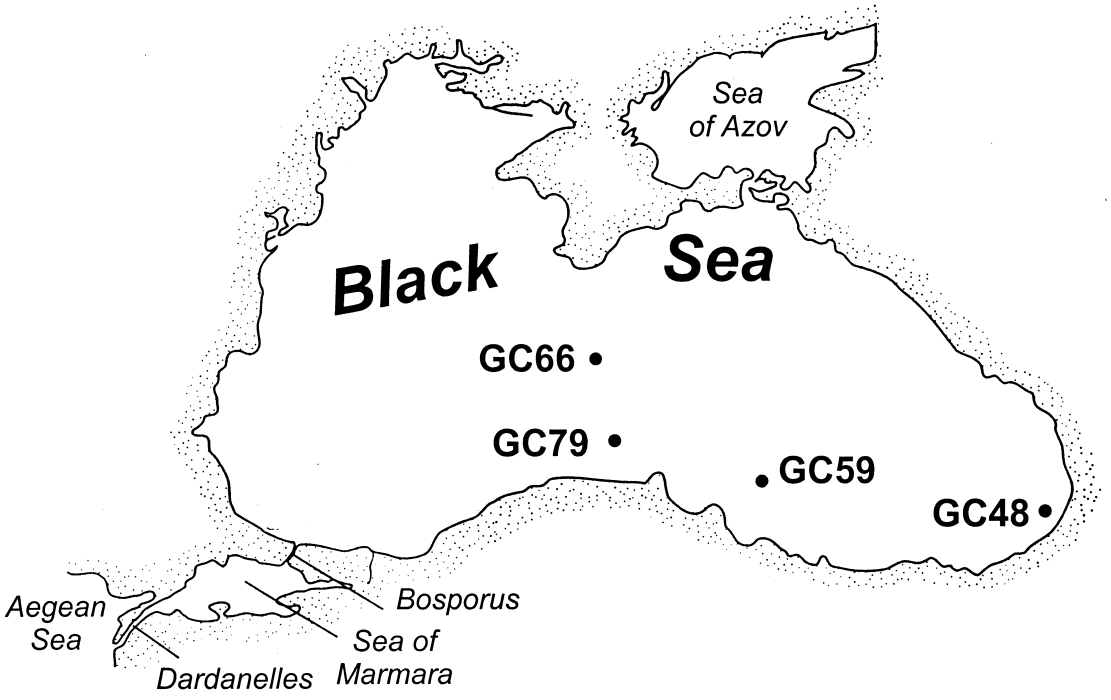

Fig. 1. Location of sediment core stations discussed in this paper. Cores collected during Leg 1 of the *RV Knorr* expedition to the Black Sea.

The results of these studies are consistent in showing that pyrite formation is limited mainly by iron availability in the most recent non-turbiditic sediments (Unit I) comprising the deep, abyssal plain of the Black Sea. Berner (1974) recognized older sediments (in Unit III) that are black colored and rich in iron monosulfides (metastable precursors to pyrite), whereas the most recent carbonate-rich sediments were gray colored and rich in pyrite, rather than iron monosulfides. He suggested that these relationships were the result of an upward increase in salinity and consequent availability of sulfate, evidently required for the complete conversion of iron monosulfide to pyrite. Apparently pyrite formation in modern Black Sea sediments or underlying sapropels of Unit II is not limited by the availability of organic carbon or sulfate. Evaluations of iron partitioning in Unit I sediments support this conclusion and point to reactive iron as the main control on pyrite concentrations (e.g., Lyons and Berner, 1992). The same general pattern of reactive iron control on the formation of pyrite is found in Unit II (Calvert et al., 1996; Wilkin et al., 1997). Calvert et al. (1996) and Wilkin et al. (1997) showed that in the lower part of Unit III (e.g., at least 50 cm below the Unit II-III boundary), concentrations of organic carbon and pyrite are low, but reactive iron is abundant. The C/S ratios of these early Unit III sediments suggest that pyrite formation was limited by the supply of dissolved sulfate, organic carbon, or both. Therefore, over a relatively short interval of time (< 15 ka), depositional environments have varied in the Black Sea such that the dominant controls on pyrite formation have fundamentally changed.

3. METHODS

The sediment gravity cores studied here were collected during Leg 1 of the 1988 *R/V Knorr* Black Sea expedition (Fig. 1). The cores were retrieved from water depths of 205 m (GC48), 600 m (GC59), 707 m (GC79), and 2090 m (GC66). These cores were specifically chosen for our analysis of Fe-S-C relationships because they represent a continuum of depositional environments from deep, anoxic basin sediments to shallower sediments closer to the depth of the oxic-anoxic transition (the chemocline) in the modern water column. Sediments and lithologic correlation in these cores are described in detail elsewhere (Arthur and Dean, 1998). Some of the data for core GC59 were reported previously in Wilkin et al. (1997); however, for the present study cores, GC48 and GC59 were resampled from the cold archives at the Woods Hole Oceanographic Institution. The cores preserve details of sedimentation in Units I, II, and III. Consequently, they provide a record of anoxia development in the Black Sea basin. Core logs suggest undisturbed sedimentation and records of Unit I to Unit III deposition in cores GC48, GC59, and GC79. In the deepest core, GC66, only a thin 5 cm section of Unit I is present, and the boundary between Unit I and Unit II is marked by a ~25 cm thick homogeneous turbiditic mud. A separate turbidite appears at a depth of ~78 cm. See Arthur and Dean (1998) for correlations and lithologic details.

Organic and carbonate carbon were determined using a Coulometrics Coulometer System 140 on powdered samples at selected depth intervals. Total iron, aluminum, and titanium in the sediments were determined by using inductively coupled plasma-atomic emission spectrometry (ICP-AES, Leeman Labs PS3000) after fusion and acid digestion (GC48, GC59 Unit I), or by wavelength dispersive X-ray fluorescence (XRF) spectrometry on fused glass discs (GC59, GC79, GC66). The accuracy of the measurements was verified for both ICP and XRF determinations by using standard USGS reference materials; the precision of the measurements was better than 5% (2σ). The amount of reduced sulfur (pyrite S + acid-volatile S + elemental sulfur) was determined directly with a sulfur coulometer from the quantity of hydrogen sulfide released from powdered sediment samples after reaction with a boiling 1 *M* $CrCl_2$-HCl solution (Canfield et al., 1986; Suits and Wilkin, 1998). Each sample was generally run in duplicate and reported as the average of the two analyses. The quantity of Cr(II)-reducible sulfur is assumed here to be entirely composed of pyrite. Analyses for acid-volatile sulfides by reacting sediment samples with hot 6 N HCl were below detection, indicating that iron monosulfides

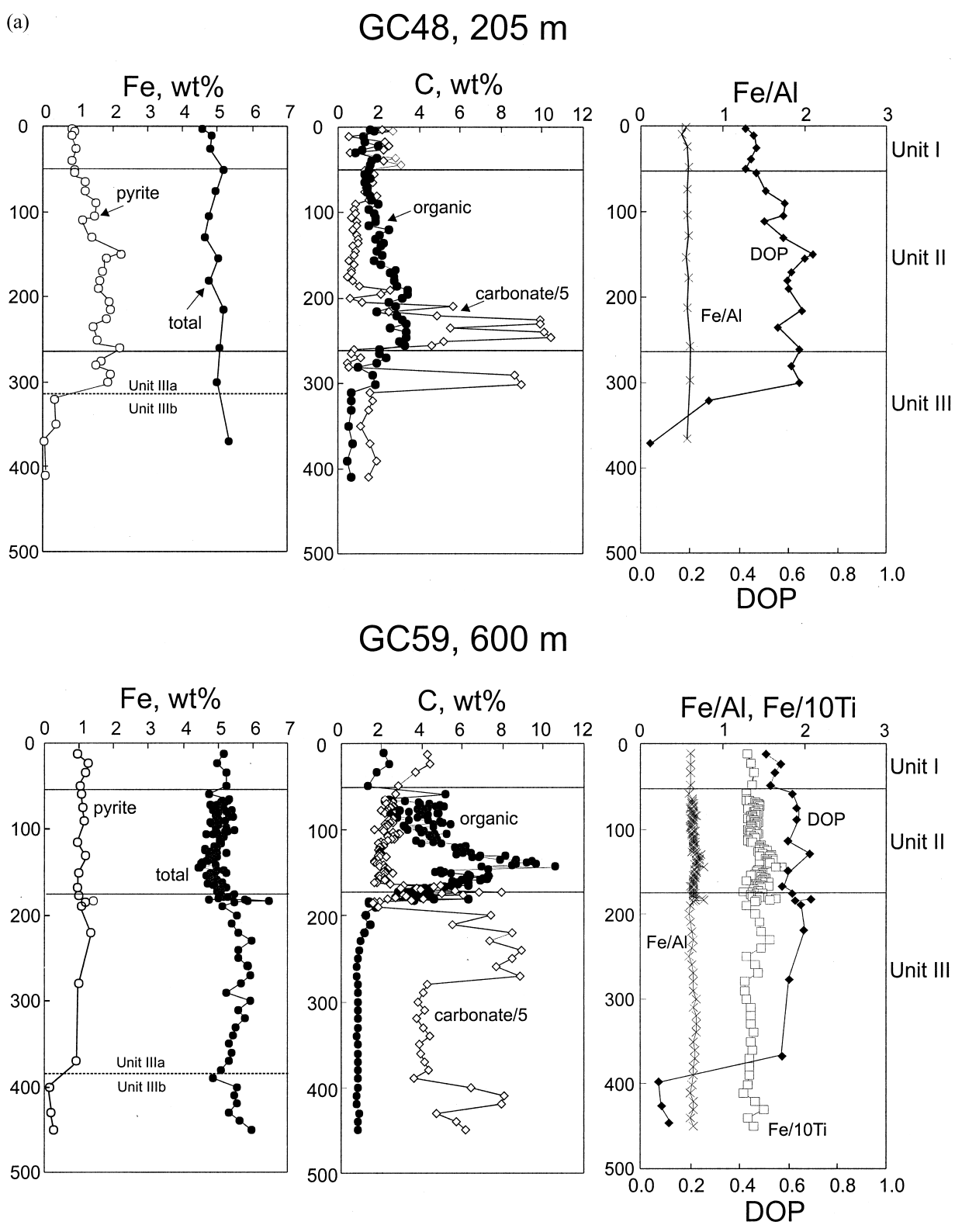

Fig. 2. Down-core distribution of sediment components in Black Sea cores GC48, GC59, CG79, and GC66. Concentrations of pyrite, total iron, and organic carbon are plotted on a carbonate-free basis.

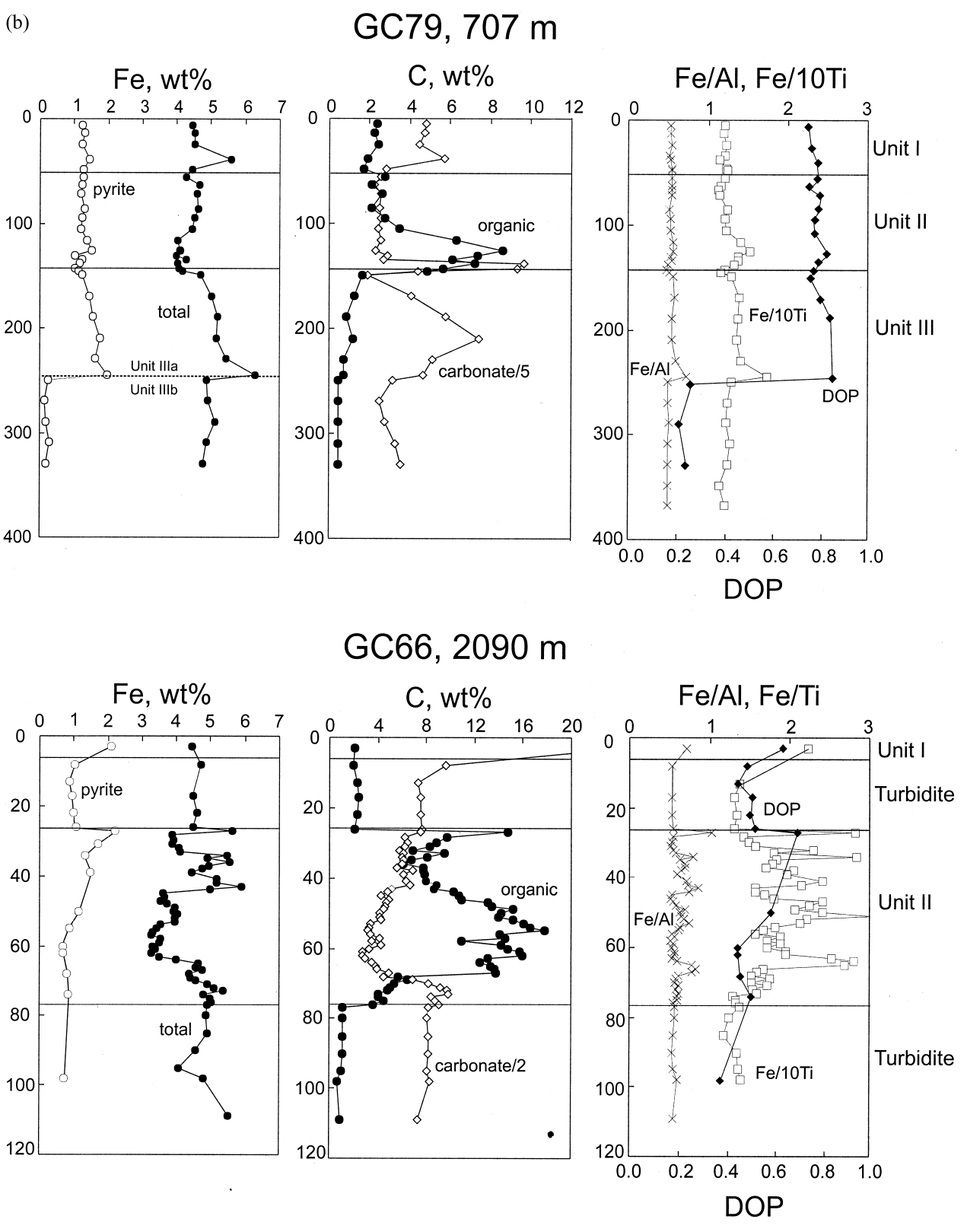

Fig. 2. (Continued)

were either not present or had oxidized to iron (oxy)hydroxides during storage.

An evaluation of Fe partitioning was carried out by using the cold HCl method of Leventhal and Taylor (1990) and the dithionite and ascorbate extractions as described by Kostka and Luther (1994). The amount of iron released from the sediments after these various leach procedures was determined, after dilution, by atomic absorption spectroscopy (Perkin Elmer 703). The overall precision of each of these extractions was found to be between 10 and 15%, based on triplicate analyses of five different sediment samples. These different leaching solutions allowed a determination of the following inorganic fractions of Fe: (1) amorphous Fe(III) oxyhydroxides (ascorbate), (2) crystalline Fe(III) oxyhydroxides (dithionite minus ascorbate), (3) leachable silicate-bound Fe (HCl minus ascorbate), and (4) sulfidized iron (Cr[II]). The amount of iron in pyrite was calculated based on the Cr(II)-reducible sulfur assuming pyrite stoichiometry. Refractory iron was determined by subtracting from total iron the amounts of amorphous oxyhydroxide, crystalline oxyhydroxide, leachable silicate-bound, and sulfidized iron. Separate extractions were performed on untreated, dried sediments. The results of these extractions were checked by sequentially extracting sediment with ascorbate, HCl, and dithionite.

The sulfur isotope composition was determined for total Cr(II)-reducible sulfur in selected samples from cores GC48 and GC66. Cr(II)-reducible sulfur was fixed as Ag_2S and then converted to SO_2 by combustion with CuO in a vacuum extraction line. The sulfur isotopic composition of the SO_2 gas was determined on a VG Prism Series II isotope ratio mass spectrometer. Sulfur isotope ratios are reported using the $\delta^{34}S$ notation as permil deviations relative to the Cañon Diablo troilite standard. Instrumental precision was always within $\pm 0.05‰$. The overall precision of the sulfur isotope determinations reported here is estimated to be $\pm 0.3‰$ (1σ), based on triplicate analyses of one sample.

Pyrite morphologies were studied and size distributions were measured by using reflected light and scanning electron microscopic techniques (Wilkin et al., 1996, 1997). Sediment samples were mounted in epoxy resin and ground and polished using diamond pastes to obtain cross sections of the sediment grains. Pyrite particle sizes were measured using a 100× objective lens and an ocular field micrometer. Approximately 50 samples were examined, and the size of at least 100 pyrite particles was determined per section.

4. RESULTS

4.1. Pyrite Iron

Depth-dependent concentrations of total iron and pyrite iron are plotted in Figure 2. The amount of pyrite contained in Unit I, on a carbonate-free basis, is remarkably uniform in all of the cores studied here (mean 0.90 wt.% Fe, $n = 50$). This average value is generally consistent with data presented in Rozanov et al. (1974), Calvert and Karlin (1991), Lyons and Berner (1992), Calvert et al. (1996), and Lyons (1997). The transition between Unit I and the organic carbon-rich Unit II is not clearly indicated by a change in pyrite concentration (Fig. 2). In Unit II, pyrite concentrations average 0.98 wt.% Fe ($n = 120$), only slightly higher than those in Unit I. Pyrite contents in Units I and II are relatively constant with depth in cores GC59, CG79, and GC66. In core GC48, however, pyrite concentrations are more variable, reaching values as high as 2.1 wt.% Fe in Unit II. In cores GC59 and GC79, pyrite distributions in the upper horizons of Unit III are again relatively uniform and similar to those in Unit I and Unit II. However, pyrite concentrations in these cores decrease abruptly at 370 cm and 250 cm, respectively, to values below 0.30 wt.% Fe. For the purposes of this study, in the following sections, Unit III is informally divided (Fig. 2) based on this break in pyrite abundance, into Unit IIIa (upper pyrite-rich) and Unit IIIb (lower pyrite-poor). In core GC48, this transition to lower pyrite contents (Unit IIIb) is more gradual and begins at 320 cm, or ~55 cm below the Unit II-III boundary.

The IIIa–IIIb differentiation is informal at best, as there is no distinct lithologic feature that would lead to a more formal designation. The primary difference is, as stated above, pyrite content. In freshly opened cores, however, we did observe distinct dark gray to black layers at and below the nominal IIIa-IIIb horizon in GC59 and GC79 and in many other cores. For example, the dark bands in GC79 commenced at ~245 cm depth in the core and continued to ~280 cm. The top of the dark banding corresponded very closely to the abrupt decrease in DOP in GC79. The dark banding faded rapidly upon exposure to the atmosphere, and we suspect that this represents coloration imparted by metastable iron monosulfides, as suggested by Berner (1974). As discussed later, the thickness of Unit IIIa changes systematically with water depth and is probably related to the depth of postdepositional penetration of a sulfide "front."

4.2. Pyrite Morphologies and Framboid Size Distribution

Textural forms of pyrite in Black Sea sediments shown in Figure 3 include framboids, filled-in framboids, single crystal euhedral grains (<10 μm), and fine- to coarse-grained (<35 μm) anhedral masses (Table 1). In Unit I and Unit II, framboids represent the dominant textural form of pyrite in all of the cores studied (Fig. 4 and Table 1). In all Unit I and Unit II samples from GC59, GC79, and GC66, >86% of the pyrite particles observed had framboidal morphology; in Unit I, generally >90% of pyrite particles were framboids. The individual microcrystals composing the framboids were generally <1 μm in diameter and usually displayed pyritohedral or octahedral forms. In Units I and II of GC48, the proportion of nonframboidal forms is comparatively greater than in the deeper water cores, and single, non-aggregated crystals with octahedral or pyritohedral forms were common and always <5 μm in diameter (Table 1). In Unit IIIa, framboids again represent a major textural component. However, the proportion of euhedral and anhedral grains relative to framboids increases below the Unit II–III boundary. In Unit IIIb, or below the top 50 to 150 cm of Unit III, framboids are rare, and pyrite grains are scarce, fine- to coarse-grained particles with or without displaying euhedral forms (Table 1).

A comparison of framboid size distributions in Units I, II, and III is shown in the box-and-whisker plots of Figure 5. The maximum framboid diameters observed were 19 μm and 15 μm in Unit I and Unit II, respectively, and ~80% of all framboids in these units were <5 μm. These size characteristics are significantly different from those of Unit IIIa, where 50 μm framboids are present, and 20% of the framboids are >12 μm. In Unit I, there is an apparent correlation between maximum framboid size and water depth to the sediment-water interface, with the deepest core showing the narrowest framboid size range (Fig. 5).

In Unit II of core GC48, there are two depth intervals with anomalous maximum framboid diameters compared to the Unit II trends observed in GC48 and in the other cores, i.e., at depths of ~110 cm and 170 cm. In these depth intervals, framboid diameters reach up to 30 μm or approximately 2× the maximum size typically encountered in Unit II. These depth inter-

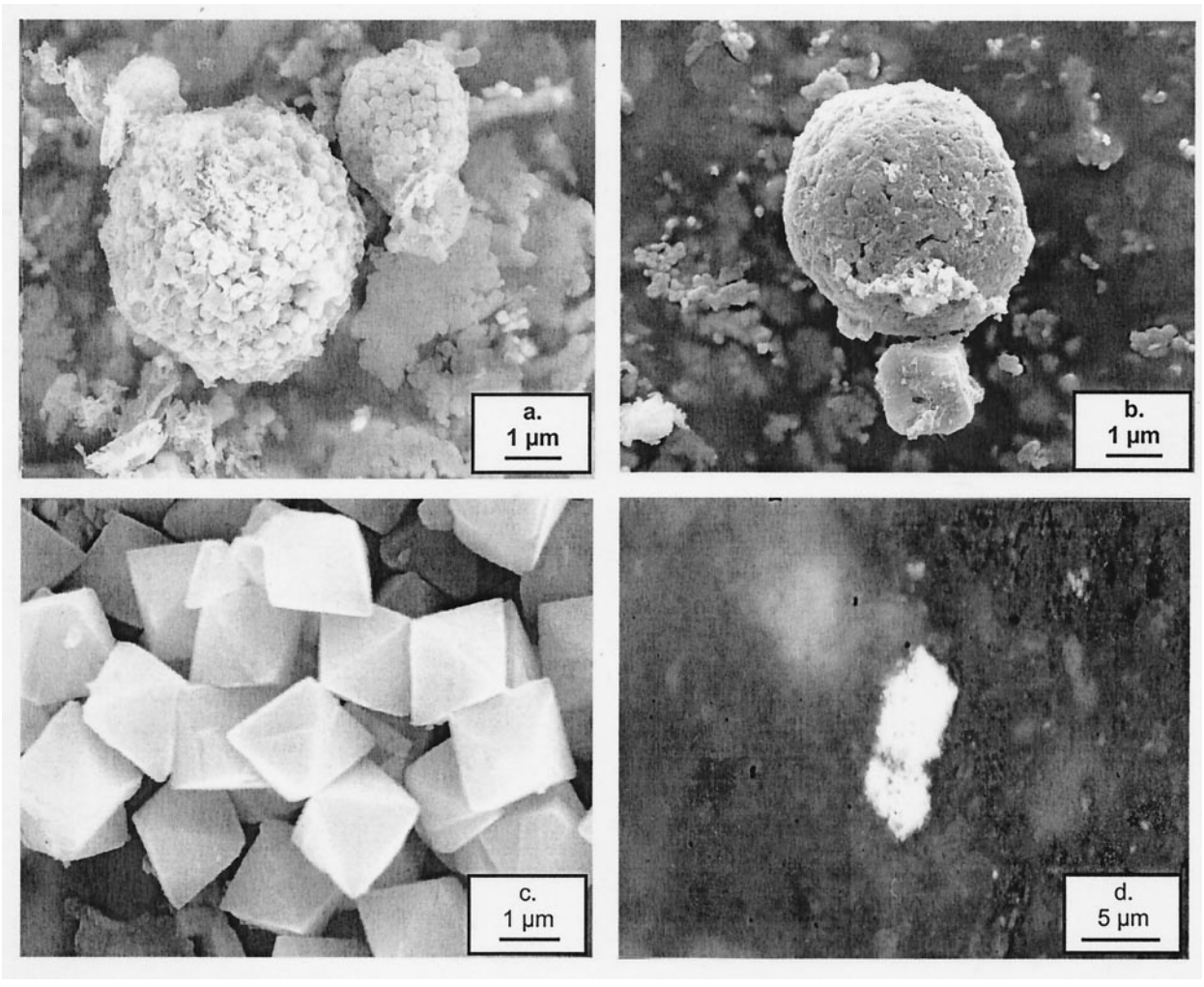

Fig. 3. Photomicrographs of pyrite textures: (a) framboids (Unit I, GC59), (b) filled-in framboid (Unit II, GC48), (c) euhedral grains, and (d) anhedral grain (Unit IIIb, GC59).

Table 1. Pyrite texture distribution in Black Sea sediments.

Core	Depth (m)	Unit	%Framboids (unfilled)	%Framboids (filled)	%Euhedral	%Anhedral	Av. wt.% pyrite (S)
GC48	200	I	45	20	20	5	1.01
		II	50	20	20	10	1.88
		IIIa	25	10	15	50	1.51
		IIIb	–	10	20	70	0.22
GC59	600	I	90	5	5	–	1.29
		II	95	5	–	–	1.20
		IIIa	40	20	25	15	1.30
		IIIb	–	–	–	–	0.19
GC79	707	I	95	–	5	–	1.50
		II	90	5	5	–	1.41
		IIIa	15	30	35	20	1.85
		IIIb	<5	–	10	90	0.24
GC66	2090	I	90	5	5	–	2.42
		II	85	10	5	–	1.36
		Turbidites	5	35	10	50	1.16

Note: Percentages are based on number of particles observed and do not necessarily reflect mass or volume distributions of the different textural types. Pyrite concentration is on a carbonate-free basis.

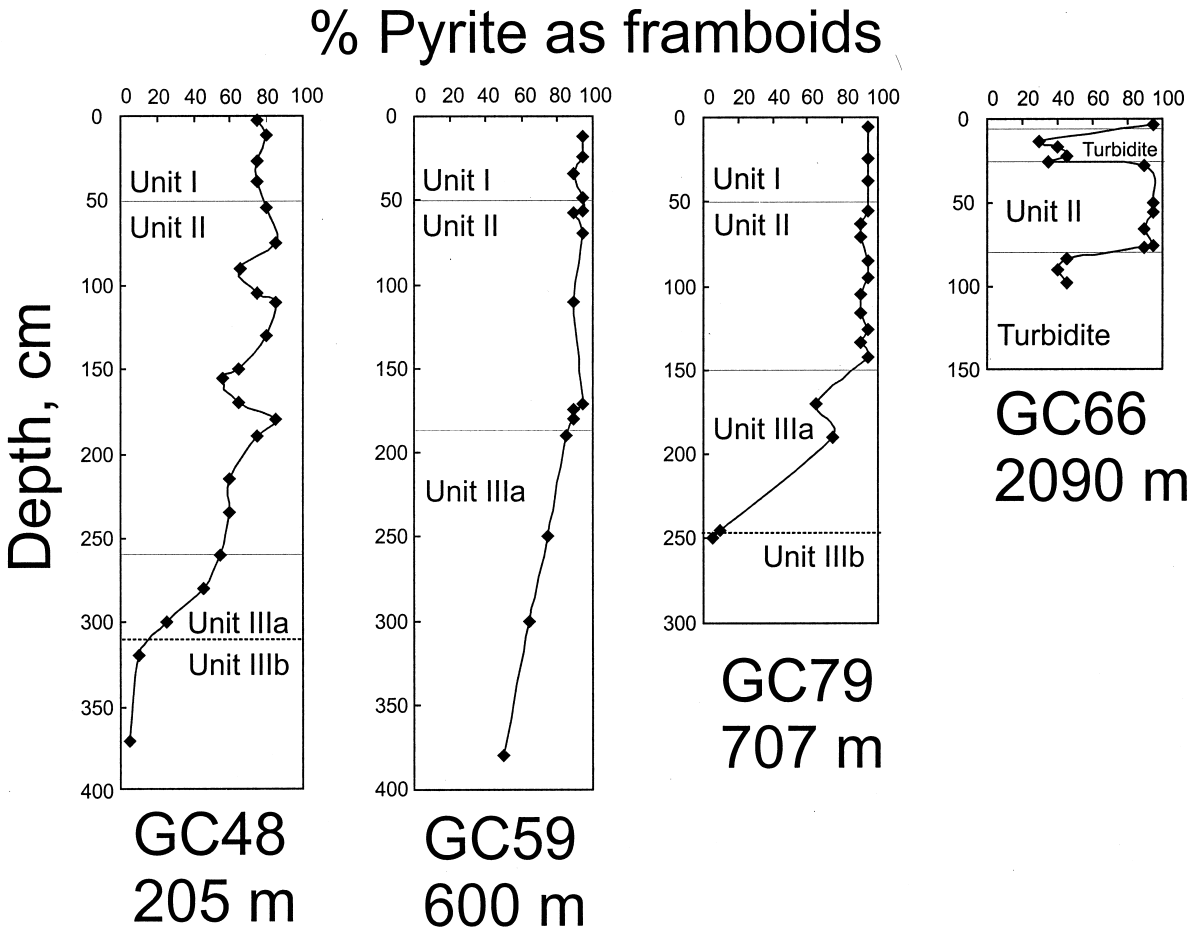

Fig. 4. Down-core distribution of %pyrite as framboids (unfilled + filled) in Black Sea cores GC48, GC59, GC79, and GC66.

vals in GC48 correspond to the depths at which sediment fabric consists of discontinuous laminations with patches of burrow mottling.

Pyrite contained in the mud-turbidite layers (Fig. 3) in core GC66 is present mainly as anhedral masses and as spherical particles considered to be filled-in framboidal aggregates (Wilkin and Barnes, 1997b). The particles are up to 25 μm in diameter, and the size distribution of these particles generally falls between that observed in Units I and II and that in Unit IIIa (Fig. 6). Absent in the Black Sea turbidites are the large, polyframboidal aggregates (up to 400 μm) documented in several Paleozoic graywackes and interpreted as the product of seafloor sediment reworking (e.g., Love, 1971).

4.3. Iron Partitioning

With one exception, iron in pyrite represents ~25% of the total amount of iron present. The exception is Unit IIIb, where pyrite iron values are low, and pyrite iron makes up only ~4% of the total sedimentary iron budget. The amount of total iron in the surface sediments, on a total sediment basis, tends to decrease with increasing water depth or distance from the shore. However, when total iron values are calculated on a carbonate-free basis, total iron in the most recent sediments of Unit I varies in a narrow range from ~4.5 to 5.1 wt.% regardless of geographic position (Fig. 2).

The amount of HCl-soluble iron (carbonate-free) tends to decrease from Unit I (0.94 ± 0.20 wt.% Fe, $n = 11$) to Unit II (0.77 ± 0.23, $n = 53$) and Unit IIIa (0.59 ± 0.26, $n = 12$). Consequently, because of the relatively constant pyrite concentrations in these sediments as described above, DOP values are slightly lower in Unit I compared to those in Unit II and Unit IIIa (Table 2), where DOP (Berner 1970) is expressed as: $Fe_{py}/[Fe_{py} + Fe_{HCl}]$.

There are no significant discontinuities in DOP values at the Unit I–II or Unit II–III boundaries. In Unit IIIb, however, the amount of HCl-extractable iron approximately doubles, and DOP values are <0.20 (Table 2). With the exception of core GC79 and Unit II of core GC66, DOP values in Unit I and Unit II tend to increase with increasing water depth or distance from shore. Core GC79 displays anomalously high values of DOP, both in Unit I and Unit II, compared to the general distribution of DOP values of surficial sediments contoured by Canfield et al. (1996). The turbidite layers in core GC66 have low DOP values of 0.47 ± 0.05, similar to those in Unit I of the shallowest core GC48 (0.44 ± 0.02). See Table 2 and Lyons (1997).

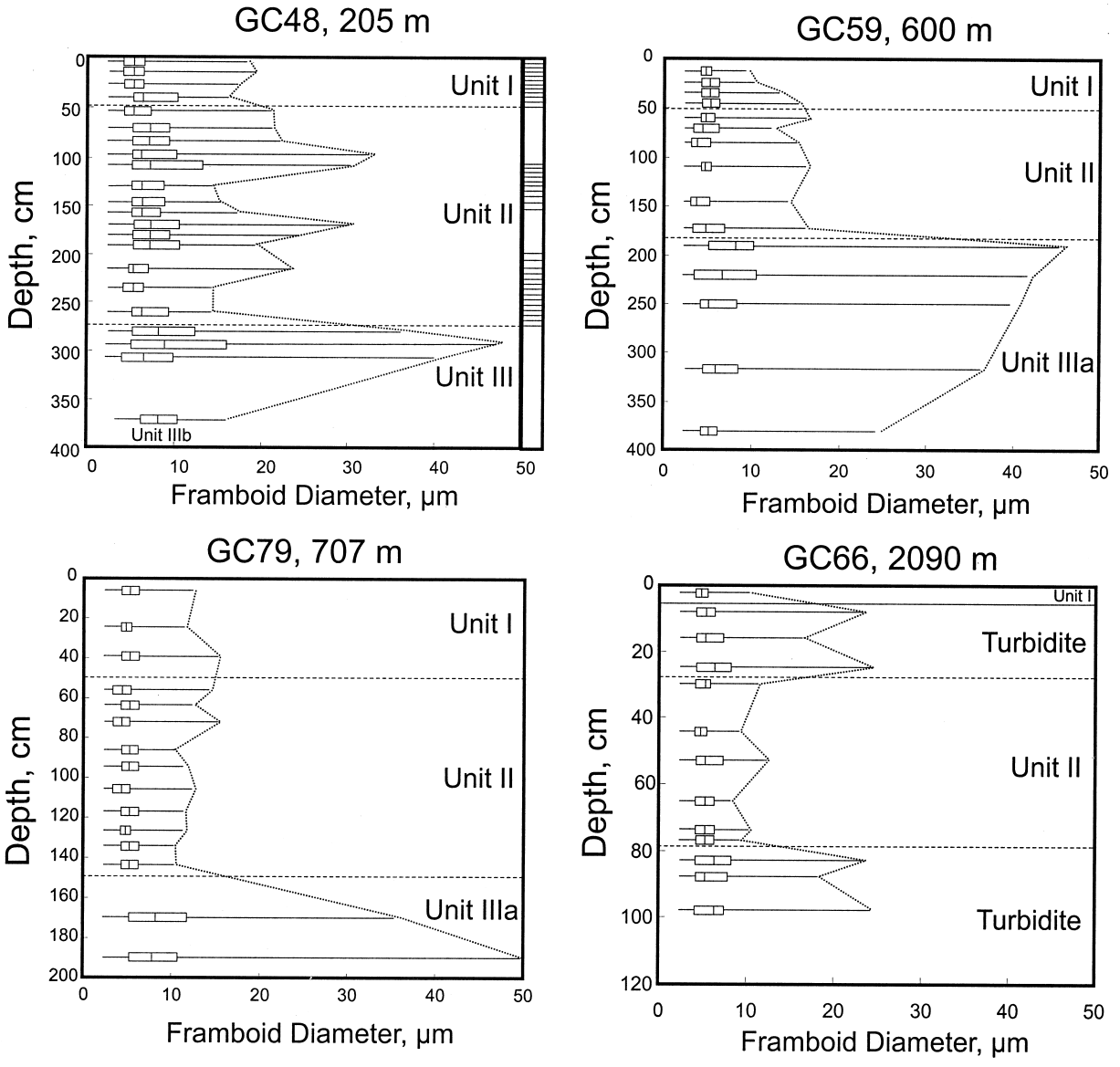

Fig. 5. Box-and-whisker plots showing down-core framboid size distributions from Black Sea cores GC48, GC59, GC79, and GC66. The boxes extend from quartile Q = 0.25 to quartile Q = 0.75. The median value is marked in each box. The lines extending to the right and left of each box delineate maximum and minimum values, respectively.

The results of the ascorbate, dithionite, and HCl extractions on cores GC48, GC79, and GC66 indicate that the residual iron component is the largest fraction of total sedimentary iron, except in the carbonate-rich Unit I sediments of GC66 (Fig. 7). The amount of Fe leached by ascorbate, analytically defined as the amorphous ferric (oxy)hydroxide fraction, is relatively constant and independent of depth in all cores (0.12 ± 0.05 wt.%, $n = 28$). It is probable that at least some of this component represents iron monosulfides that oxidized during sample storage. The amounts of crystalline ferric oxyhydroxide and leachable silicate-bound Fe do not vary much with depth in Units I, II, and IIIa, although there are apparent slight enrichments in the oxyhydroxide/oxide component in the top 30 cm of cores GC48 and GC79 and in the lower part of Unit IIIb. The persistence with depth of dithionite-extractable iron suggests

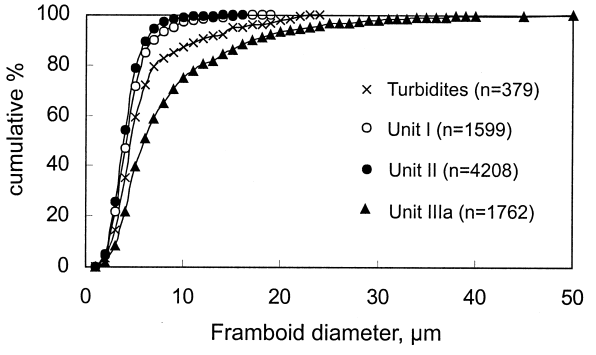

Fig. 6. Cumulative framboid size distributions for Unit I, Unit II, Unit IIIa, and turbidites.

Table 2. DOP values for Black Sea sediments.

	GC48	GC59	GC79	GC66
Unit I	0.44 ± 0.02	0.53 ± 0.02	0.66 ± 0.02	0.63 ± 0.00
Unit II	0.59 ± 0.06	0.62 ± 0.04	0.72 ± 0.03	0.52 ± 0.10
Unit IIIa	0.63 ± 0.03	0.62 ± 0.04	0.78 ± 0.02	–
Unit IIIb	0.16 ± 0.11	0.09 ± 0.02	0.26 ± 0.03	–
Turbidites	–	–	–	0.47 ± 0.05

Reported uncertainties correspond to 1 s.d. about the mean DOP value.

that the techniques used here for determining iron partitioning, in fact, yield more iron than is sulfidized in the sediment, even over time periods $>$ 7 ka.

4.4. Fe-S-C Systematics

When viewed collectively, there is no apparent relationship between the abundance of organic carbon and pyrite sulfur in Black Sea sediments (Fig. 8a). More specifically, the linear trend typical of most normal oxygenated marine sediments is not followed (Berner, 1984). Sediments of Units I and IIIa are generally enriched in pyrite at equivalent organic carbon contents compared with normal marine sediments, whereas data from Unit II are widely scattered but may be either pyrite-depleted or pyrite-enriched (Fig. 8a). Note that the Unit I sediments analyzed here are generally depleted in organic carbon but contain pyrite concentrations similar to those described in other recent studies (e.g., Calvert and Karlin, 1991; Lyons and Berner, 1992; Calvert et al., 1996). The mud turbidites cluster in a narrow region marked on Figure 8a, slightly above the normal marine line. Sediments of Unit IIIb are distinctive from overlying sediments. The low concentrations of pyrite in these sediments could be the result of limitations in either sulfur or organic carbon.

The relationship between carbonate-free total Fe and organic carbon in Figure 8b suggests that the factors controlling accumulation of these variables are decoupled (Fig. 8b). The general trend of data in Figure 8b agrees well with a dilution curve, modeled by progressive dilution by organic carbon, of a source sediment with an assumed total Fe concentration of 5.5 wt.%. The relationships between total Fe and pyrite Fe shown in Figure 8b again show that the amount of pyrite in Black Sea sediments is not clearly linked to organic carbon concentrations but is instead consistently ~25% of the total sedimentary iron concentration (pyrite field in Fig. 8b). This relationship reflects iron-limited conditions of pyrite formation with the amount of pyrite Fe fixed by the iron reactivity of the ultimate source material supplied to the basin.

4.5. Sulfur Isotopes

The $\delta^{34}S$ values of pyrite in cores GC48 and GC66 are listed in Table 3. In shallow water core GC48, values of $\delta^{34}S$ for pyrite range widely between −38.0‰ and +11.0‰ (Fig. 9a). Pyrite becomes more enriched in ^{34}S with increasing depth in the GC48 core. In Unit I, $\delta^{34}S$ values are fairly uniform and depleted in ^{34}S (mean = −37.3 ± 0.7‰, n = 5), and in

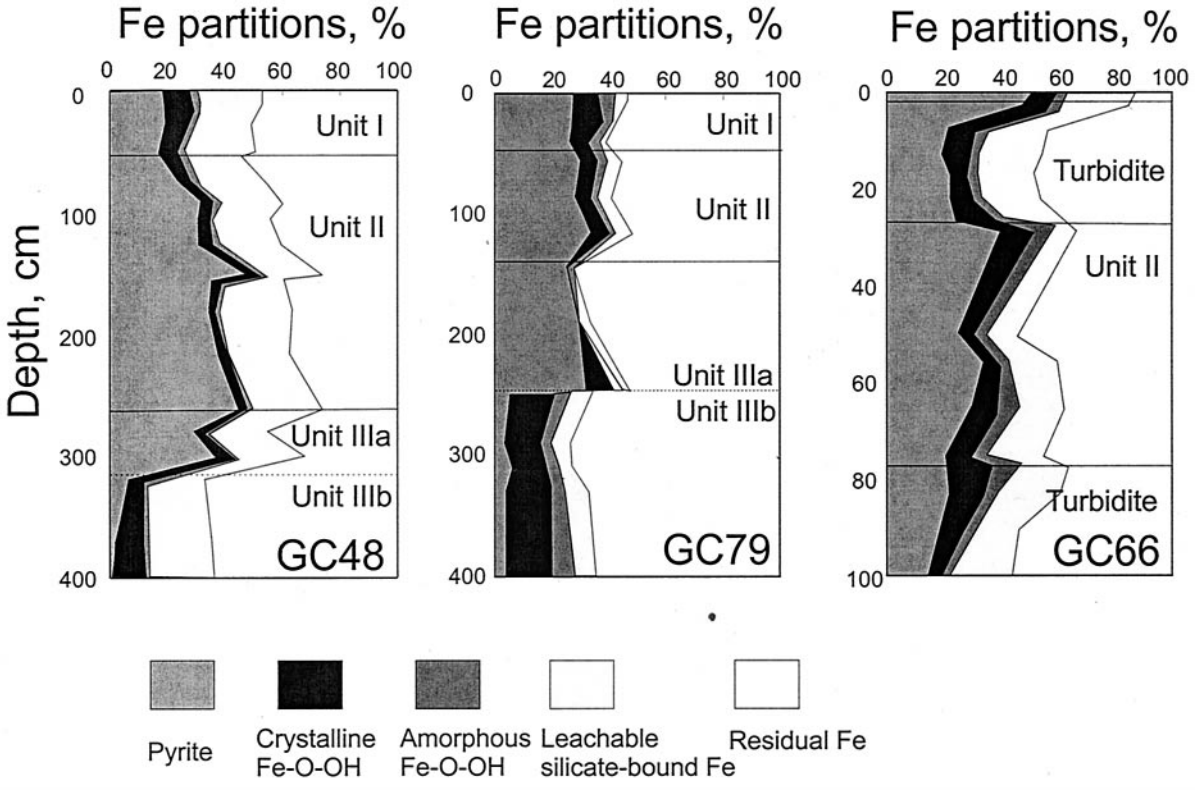

Fig. 7. Down-core distribution of solid-phase iron partitions in Black Sea cores GC48, GC79, and GC66.

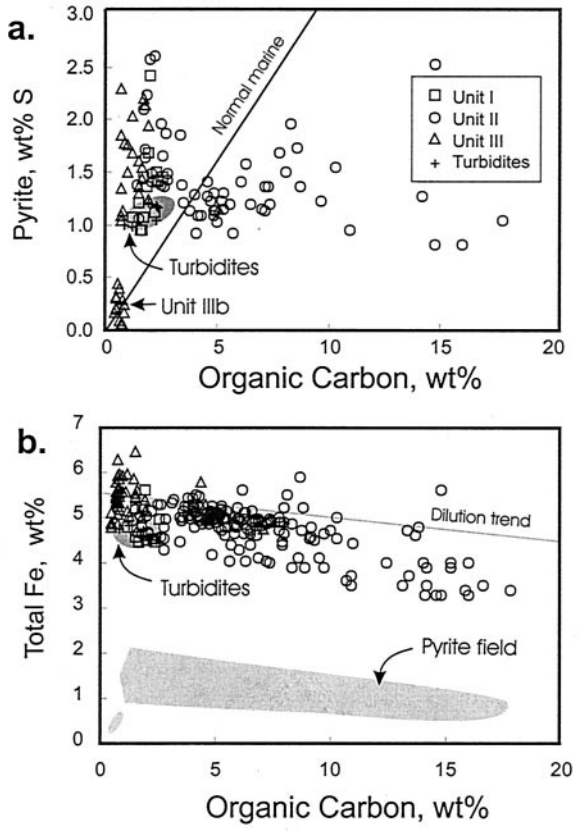

Fig. 8. Relationship between (a) pyrite S and organic carbon and (b) total Fe and organic carbon, carbonate-free basis. Normal marine line corresponds to C/Pyrite S = 2.8 (Berner 1970). The pyrite field shows the fraction of total iron contained in pyrite.

Table 3. Sulfur isotope compositions of pyrite in cores GC48 and GC66.

	δ^{34}S (‰)	Depth (cm)
GC48		
Unit I	−36.3	2.5
	−36.8	11.5
	−36.0	26.5
	−37.2	39.5
Unit II	−38.3	54.5
	−38.1	75.5
	−38.4	90.5
	−38.8	105.5
	−38.6	110.5
	−37.9	130.5
	−35.6	150.5
	−37.0	155.5
	−34.3	170.5
	−34.2	180.5
	−33.1	190.5
	−31.4	215.5
	−28.6	235.5
Unit III	−23.7	280.5
	−15.7	300.5
	−20.1	320.5
	10.9	350.5
	10.2	390.5
GC66		
Unit I	−35.2	3.0
Turbidite	−25.1	8.0
	−23.3	13.0
	−20.9	17.0
	−21.6	22.0
	−20.2	26.0
Unit II	−35.9	28.0
	−35.5	30.0
	−34.2	35.0
	−32.1	39.0

excellent agreement with the average Unit I value reported by Lyons (1997). In Unit II (GC48), however, δ^{34}S values increase progressively with increasing depth, from −35.3‰ at 55 cm to −22.5‰ at 260 cm (Fig. 9a). In the upper part of Unit III, δ^{34}S values are variable (−19.2 ± 3.3‰, n = 4), but then increase abruptly to positive values below 350 cm (Unit IIIb), corresponding to the depth where pyrite concentrations fall below 0.3 wt.%. The data obtained in deep-water core GC66 are similar for Unit I and the upper portion of Unit II. However, in core GC66, δ^{34}S values in the mud turbidite are ~10‰ greater than in the immediately overlying and underlying laminated sediments (Fig. 9b). Within the turbidite, δ^{34}S values decrease slightly with increasing depth from −25.2‰ at 8 cm depth to −20.2‰ at 25 cm depth. In the discussion below, these trends in sulfur isotope ratios of pyrite are compared with a compilation of measurements extracted from the literature that include the water column ΣH_2S, sediment trap material, as well as sedimentary pyrite from Units I, II, and III.

5. DISCUSSION

5.1. Pyrite Texture and Size Distribution

In near-surface environments, O_2/H_2S redox transitions are important sites for Fe-S-C cycling and the formation of iron monosulfides and iron disulfides. In the modern Black Sea, this redox interface occurs near the base of a steep halocline at ~80 m in the center of the basin but deepens to about ~150 m along the basin margins. A natural distinction was noted by Raiswell and Berner (1985) between water column-formed pyrite (syngenetic) and pyrite added below the sediment-water interface (diagenetic). Studies of Fe-S-C relationships (e.g., Leventhal, 1983; Lyons and Berner, 1992), S-isotope systematics (e.g., Muramoto et al., 1991; Lyons, 1997), and pyrite morphology and size distribution (Wilkin et al., 1996, 1997) all point to a pyrite burial flux in the deep water Black Sea sediments dominated by water column inputs, i.e., the syngenetic component.

On the basis of laboratory experiments, Wilkin and Barnes (1996) documented a progression of pyrite morphologies, from fine-grained crystals to framboidal aggregates, that correlate with increasing rates of pyrite nucleation. In experimental systems with high sulfide oxidation rates, generated by bubbling air through NaHS solutions containing suspensions of iron monosulfide colloids, these authors found an increased tendency to form framboidal aggregates and fast iron monosulfide-to-pyrite conversion rates. In more reducing, alkali polysulfide solutions, iron monosulfide-to-pyrite conversion rates were comparatively slow, and euhedral crystals developed rather than framboids. In all experiments, solution compositions were saturated with respect to iron monosulfide solubility, so the type and concentration of oxidizing species present controlled nucleation rates. These findings are consistent with

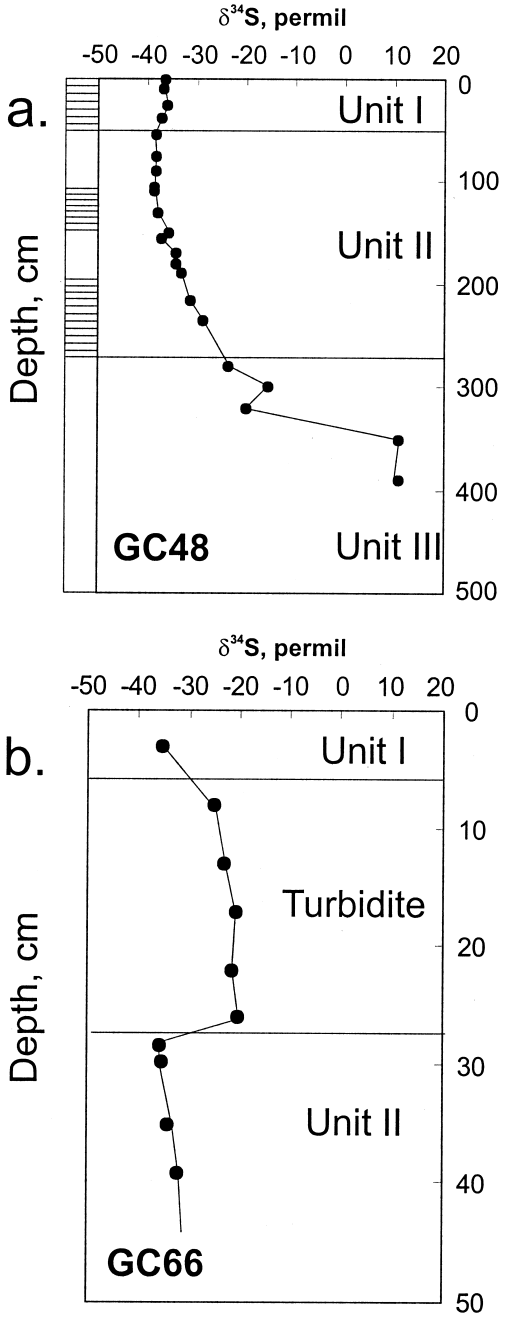

Fig. 9. Depth distribution of pyrite $\delta^{34}S$ values in Black Sea cores (a) GC48 and (b) GC66.

observed dominance of framboidal pyrite in deep basin Unit I sediments that originated in the water column, subjacent to the O_2-H_2S transition. The dominance of syngenetic framboidal pyrite in deep basin Black Sea sediments requires an availability of ΣH_2S, suitable electron acceptors to facilitate the formation of the critical intermediate sulfur species, and a supply of reactive iron that is nearly completely exhausted, i.e., sulfidized in the overlying water column. If reactive iron was effectively transported through the chemocline and deposited in underlying sediments, reducing conditions there would favor the diagenetic formation of euhedral crystals of pyrite, and framboidal forms would be comparatively less abundant.

In Units I and II of the shallowest core (GC48), the proportion of pyrite particles as framboids is lower than in GC59, GC79, and GC66 (Fig. 4). This reduced abundance of framboidal pyrite may reflect a syngenetic flux that is made up of both framboids and euhedral grains or an increased diagenetic burial flux of pyrite in this shallow core as supported by STA 15 data in Lyons (1997). The latter is at least partly supported by the increased amount of framboid infillings in both Units I and II of GC48. Infilled framboids are frequently observed in modern and ancient sediments and apparently are the result of surface nucleation and continued pyrite growth on framboids within the sediments (e.g., Love and Amstutz, 1966; Wilkin and Barnes, 1997a). Because framboidal aggregates are comprised of cubic, close packed arrangements of monodisperse microcrystals, they have a void space of ~26%. If a distribution of framboids were completely filled with pyrite without any change to the aggregate diameter, the maximum mass increase of pyrite in a sediment would be ~33%, which is less than the observed relative increase in pyrite concentration in GC48 through Units I and II.

On the other hand, if pyrite formation has continued below the sediment-water interface and below the O_2-H_2S boundary in GC48, the additional pyrite could also represent diagenetic nucleation events. However, in terms of a reaction pathway for pyrite formation, the identity of the reactive oxidant is equivocal. Typically, the O_2-H_2S interface is the site of production of sulfur intermediates, like elemental sulfur and polysulfides (Jørgensen et al., 1991), which react with iron monosulfides to form pyrite. In addition to sulfur intermediates, oxygen is also available for reaction to form pyrite near O_2-H_2S transitions by diffusive and advective processes. Apart from the production of sulfur intermediates, oxygen appears to directly increase the rate of iron monosulfide-to-pyrite transformations by forming reactive centers on the surfaces of precursor particles (Wilkin and Barnes, 1996; Benning et al., 2000). Sulfur intermediates, however, may also form below O_2-H_2S boundaries by reactions between hydrogen sulfide and the surfaces of Fe and Mn oxide particles settling through the water column (Millero, 1991) or progressively buried below the sediment-water interface. For example, Pyzik and Sommer (1981) investigated reactions between hydrous iron oxides and aqueous sulfide species and evaluated the kinetics and mechanisms of iron monosulfide precipitation. The reaction pathways in their experiments followed overall reactions of the type:

$$2FeOOH + HS^- + H_2O = S° + 2Fe^{2+} + 5OH^-. \quad (1)$$

Their results (see also Rickard, 1974; dos Santos and Stumm, 1992) generally show that ferric-bearing minerals will react with hydrogen sulfide to produce Fe^{2+} and some sulfur species with an oxidation state intermediate between sulfate and sulfide, depending on factors such as pH, total sulfide concentration, and ionic strength. Pyzik and Sommer (1981) identified elemental sulfur, thiosulfate, and polysulfide species as reaction products in addition to Fe^{2+}. Note that Eqn. 1 produces more Fe^{2+} than S°. Consequently, insufficient molar quantities of S intermediates become available to completely convert iron monosulfides to pyrite. A short-term buildup of iron monosulfides

over pyrite might be expected, as is typical of many euxinic basins and other sedimentary environments with fast rates of sedimentation (e.g., Boesen and Postma, 1988; Gagnon et al., 1995; Wilkin and Barnes, 1997a; Suits and Wilkin, 1998; Hurtgen et al., 1999). Sedimentary iron monosulfides such as mackinawite and greigite are thermodynamically unstable relative to pyrite or pyrite plus pyrrhotite (Berner, 1970); consequently, pyrite formation is inevitable under the reducing conditions below O_2-H_2S transitions, and will proceed slowly by iron loss following (Wilkin and Barnes, 1996):

$$2FeS + 2H^+ = FeS_2 + Fe^{2+} + H_{2(g)}. \quad (2)$$

The apparent increased diagenetic burial flux of pyrite in GC48 contrasts with the deep basin sediments as noted above. The partitioning of pyrite into syngenetic and diagenetic components is common to smaller euxinic basins such as the Pettaquamscutt River estuary (Wilkin and Barnes, 1997a) and Green Lake (Suits and Wilkin, 1998) and ultimately is related to a more refractory composition, increased sedimentation rates, and decreased surface reactivity of iron detritus near the basin margin compared to the basin center. Pyrite formation via the hydrogen sulfide pathway (Rickard, 1997) may account for the secondary accumulation of diagenetic pyrite in GC48. Although the rate of this pyrite-forming pathway is disputed under strictly anoxic conditions based on the results of laboratory studies (e.g., Wilkin and Barnes, 1996; Rickard, 1997; Benning et al., 2000), the hydrogen sulfide pathway may result in the slow formation of pyrite as euhedral grains and framboid infillings in sediments below anoxic-sulfidic water columns.

The boundary between Units II and III is clearly marked in all cores by an increase in average framboid size and framboid size variability (Fig. 5). Shown in Figure 6 is a cumulative size distribution diagram with combined data from Units I, II, and III, but excluding data from Units I and II of GC48. The framboid size distributions in Units I and II from all plotted sites are virtually identical. However, the cumulative trend in Unit I is slightly skewed to larger sizes compared to Unit II, perhaps indicative of the overall increase in water column salinity and density over the past ~1.5 ka. In other words, increased density of the water column allowed framboids forming at or near the chemocline to grow somewhat larger before falling out of the water column. There is a very distinct contrast in framboid size distribution between the laminated Units I and II sediments and Unit III. The framboid size distribution data indicate the persistence of water column anoxia throughout the deposition of Units I and II. However, they do not constrain the thickness of the anoxic water mass. The comparatively larger mean framboid size and increased size variability in Unit III sediments are consequences of pyrite framboid formation below the sediment-water interface and relate to kinetic factors associated with framboid nucleation and growth (Wilkin et al., 1996, 1997). In all cores, the fractional amount of pyrite present as framboids in Unit III decreases with increasing depth. Framboidal pyrite is virtually absent in Unit IIIb, suggesting slow, reactant-limited pyrite nucleation as supported by the very low pyrite concentrations.

During at least two periods of Unit II deposition, the O_2-H_2S interface was apparently deeper than ~200 m, as indicated by sediment fabric. The interval from 53 to 108 cm (most of Unit IIa) in GC48 consists of olive-gray clay with indistinct, discontinuous laminations and some burrow mottling. A second interval of non-laminated to poorly laminated clay occurs from 153 to 187.5 cm (lower part of Unit IIb). These two non-laminated intervals correspond to laminated sediment in all deep basin cores. Unit I and the remainder of Unit II in GC48 are finely laminated. The non-laminated intervals in GC48 indicate that oxygen was mixed down from surface waters at least to the depth of this site over two significant periods in Unit II. When combined with previous studies (e.g., Sinninghe Damsté et al., 1993; Lyons et al., 1993), these findings indicate that perturbations in the depth of the chemocline of at least 100 m have occurred over the past ~7.5 ka. The pulses of water column oxygenation in the region of GC48 are clearly reflected in some of the geochemical and textural parameters, particularly as maxima in framboid size distribution and minima in percent pyrite as framboids (Fig. 4 and 5) and, perhaps, as maxima in DOP. They are not, however, reflected in the sulfur isotopic composition of pyrite.

5.2. Sulfur Isotopes

The sulfur isotope ratios in pyrite should provide a record of the $\delta^{34}S$ of reduced aqueous sulfur and help constrain the site and timing of pyrite formation. In core GC48, the pyrite S isotope data show a large, smooth transition from ^{34}S-enriched values in Unit IIIb to ^{34}S-depleted values in Units II and I (Fig. 9a), all within 4 m of burial (compacted). The sulfur isotope data of pyrite obtained in this study are compiled with those from some previous studies in Figure 10. The values of pyrite $\delta^{34}S$ in laminated Unit I range from −38.3‰ to −34.2‰. These $\delta^{34}S$ values overlap the upper limit of those reported for particulate-reduced sulfur collected in sediment traps (Muramoto et al., 1991) and to $\delta^{34}S$ values for dissolved sulfide in the chemocline region of the water column (Sweeney and Kaplan, 1980; Fry et al., 1991), but are significantly greater than dissolved sulfide values from the deep waters of the basin (−41‰). Calvert et al. (1996) and Lyons (1997) argued that these isotope relationships indicate that pyritization presently occurs dominantly within the water column near the O_2-H_2S boundary. Similarly, $\delta^{34}S$ data of pyrite in Unit II sediments have been interpreted to reflect long-term, water column pyrite formation (Calvert et al., 1996). Key assumptions in these conclusions are that the sulfur/isotope ratio in pyrite reflects that of ΣH_2S at the site where pyrite forms, and that $\delta^{34}S$ values of water column ΣH_2S have been invariant throughout Units II and I deposition. The framboid size distribution data above provide independent evidence that the Black Sea water column was, in fact, stratified and anoxic and furthermore, that $\delta^{34}S$ values of reduced aqueous sulfur have been fairly uniform during the deposition of Unit I and the youngest Unit II sediments.

S isotope values from the fine-grained turbiditic muds exhibit enrichment in ^{34}S compared to both the laminated sediments of Units I and II (Fig. 10) (see Calvert et al., 1996; Lyons, 1997). In addition, the $\delta^{34}S$ values of pyrite in the turbidites are very similar to those from recent muds found on the basin margins (Lyons, 1997). These relationships suggest that the turbidites are probably derived from the basin margin anoxic sediments, and that a large fraction of the available

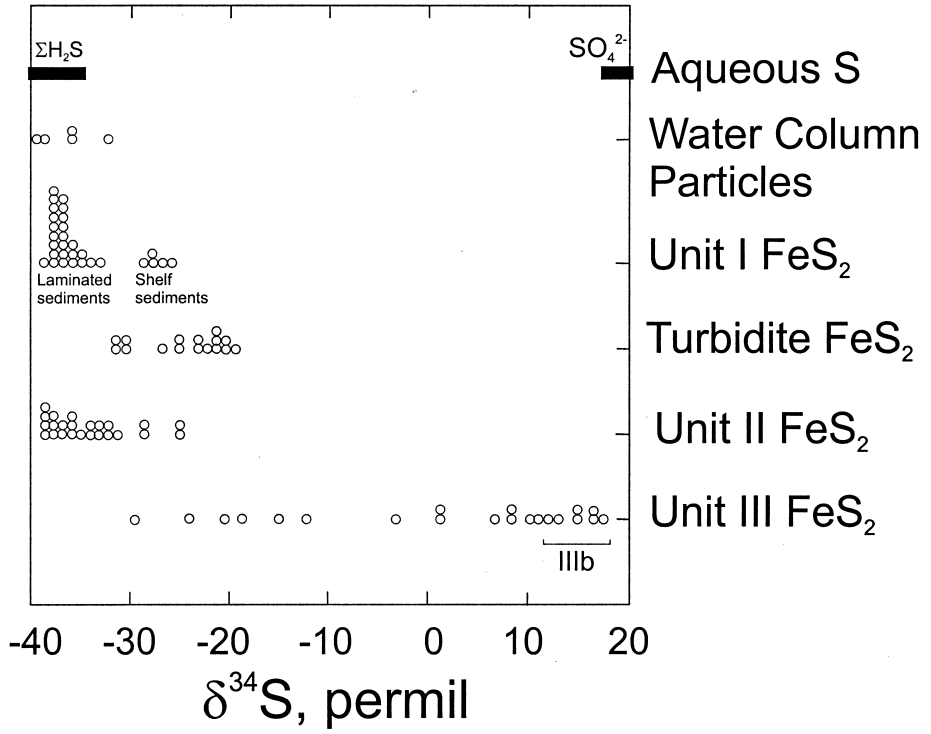

Fig. 10. Compilation of $\delta^{34}S$ values from this study and Sweeney and Kaplan (1980) for aqueous species, Muramoto et al. (1991) for particulate sulfides, Calvert et al. (1996) for pyrite, and Lyons (1997) for pyrite.

reactive iron in the turbidites was sulfidized before transport to and deposition in the deep basin (Lyons, 1997). An alternative model stems from recent observations of mud volcanoes associated with gas seeps in the central part of the Black Sea basin near the location of core GC66 (Limonov et al., 1997). In this region, mud volcanoes can be quite large, affecting areas more than 2 km in diameter. It is possible that some of the fine-grained homogeneous mud flows, generally recorded as turbidites, are in fact derived from deep sediments extruded from mud volcanoes rather than exclusively from the basin margins. Both S isotope and geochemical mass-balance considerations are permissive of the turbidites being a mixture of Units II and III sediments. However, the turbidites are clearly most similar to the marginal sediments (see Lyons, 1997).

Sediments of Unit III show the widest variability in pyrite $\delta^{34}S$ values, or −30‰ to +18‰ (Fig. 10). The heaviest values are found in Unit IIIb, where pyrite concentrations are low (<0.30 wt.% Fe). Assuming that the S isotope composition of sulfate remained constant throughout Unit III deposition, the abrupt discontinuity of $\delta^{34}S$ values coupled with the decrease in the abundance of pyrite suggest a change in the availability of sulfate. The history of pyrite formation in Unit III is discussed later in consideration of Fe-S-C relations, pyrite textures, and sulfur isotope data.

In Unit I of GC48, the average pyrite $\delta^{34}S$ value is −36.6‰, generally comparable to $\delta^{34}S$ values of pyrite in Unit I in the deep basin. In GC66, for example, pyrite in Unit I has a value of −35.2‰. However, in Unit II of GC48, $\delta^{34}S$ values of pyrite increase from −38.3‰ near the Unit I–II boundary to −28.6‰ near the Unit II–III boundary. Although sediment fabric, pyrite concentrations, DOP values, and framboid size distribution data show considerable variation through Unit II in GC48, the trend in $\delta^{34}S$ values is relatively constant. This may indicate that $\delta^{34}S$ values of pyrite are not as sensitive to changes in water column redox conditions; instead, the S isotope composition of H_2S produced and ultimately fixed in pyrite may be tied to the relative rates of sulfate reduction and sulfide oxidation (e.g., Jørgensen, 1990; Canfield et al., 1998), or may depend on downward diffusion of dissolved sulfide from the sediment-water interface or addition of sulfide produced in situ in sediment pore waters. In other words, $\delta^{34}S$ values of pyrite may not uniquely depend on whether the water column was anoxic/sulfidic, dysoxic, or oxic (Suits and Wilkin, 1998).

The trend toward more ^{34}S-enriched pyrite with depth in Unit II in GC48 is best explained by a diagenetic history that differs from other cores. As outlined above, the upper part of Unit II is characterized by $\delta^{34}S$ values that are very similar to deep basin Unit II values, which reflect pyrite formed in the water column, probably within the chemocline. However, although the lower part of Unit IIb in GC48 is finely laminated, the pyrite there is nearly 10‰ enriched relative to that in the equivalent interval in GC59. GC48 was recovered from a water depth that is somewhat deeper than the chemocline. If stability of the chemocline is assumed with respect to depth, we would expect a flux of pyrite from the water column throughout Unit II with values more depleted than −35‰, in keeping with values at other deep basin sites. The trend toward more enriched pyrite sulfur isotope values downward in Unit II may indicate a progressively greater contribution of diagenetic pyrite, which formed as the result of bacterial sulfate reduction in

the sediment. The sulfide produced by such a process would be relatively ^{34}S enriched in comparison to that produced within the water column. We observe a parallel progressive increase in non-framboidal pyrite with increasing depth in Unit II in GC48 (Fig. 6) that contrasts with the nearly constant high proportion of framboidal pyrite throughout Unit II in the deep basin cores. The increase in non-framboidal pyrite is presumably related to the addition of diagenetic pyrite formed within the sediment. Framboid size in GC48 ranges to larger diameters than in the deep basin, which suggests continued growth of framboids within the sediment after sedimentation from the water column and/or some formation and growth of framboids within the sediments. The diagenetic addition of pyrite sulfur most likely occurred because of a significantly higher sedimentation rate at GC48 in comparison to deep basin sites (see Arthur and Dean, 1998) and a lower initial DOP than in the deep basin settings. There is also a trend toward increasing DOP downcore in GC48, which we interpret as indicating progressive addition of diagenetic pyrite with time.

5.3. Limitation on Pyrite Formation

The important steps in the formation of pyrite in sedimentary or water column environments have been summarized by numerous researchers (e.g., Berner 1970, 1984; Goldhaber and Kaplan, 1974). These steps include the bacterially mediated reduction of sulfate (VI) to sulfide (−II), followed by the reaction of S (−II) as either hydrogen sulfide or bisulfide with ferrous iron to form iron monosulfide compounds and the subsequent reaction of these compounds with oxidizing reactants to form pyrite. The amount of pyrite that can accumulate in a sediment, therefore, can be limited by (1) the concentration of sulfate, (2) the amount and quality (reactive) of organic matter, (3) the amount and reactivity of iron minerals, and (4) the type and availability of oxidants (e.g., Berner, 1984). In many "normal" marine sediments, i.e., those with O_2 in the water column, the above limiting factors are manifested by a positive correlation between the abundance of pyrite and organic carbon, i.e., the amount of pyrite formed depends directly on the amount of reactive organic matter present, which covaries with concentrations of total organic carbon (Berner, 1970; Morse and Berner, 1995).

In sediments of euxinic basins, concentrations of organic carbon and pyrite are often decoupled, and plots of organic carbon vs. pyrite show positive intercepts on the pyrite abundance axis. This lack of correlation between the concentrations of organic carbon and pyrite observed in the Black Sea, and especially the positive S-intercept, has been widely used for distinguishing sedimentary rocks formed under anoxic vs. euxinic conditions from those formed under oxygenated conditions (e.g., Leventhal, 1983; Raiswell and Berner, 1985). The conventional interpretation of a C-S plot such as the one in Figure 5a suggests a system where pyrite formation is mainly syngenetic and limited by reactive iron. The decoupling of Fe and C deposition indicates that the factors controlling the flux of these components to the sediment-water interface are unrelated. In addition, DOP measurements consistently show that pyrite formation is iron-limited. Such Fe limitation is characteristic of anoxic basins where pyrite formation can take place in the water column, and reactive iron minerals are continually

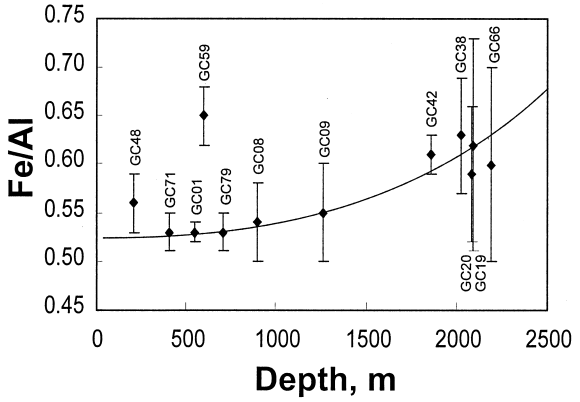

Fig. 11. Mean value (±1 s.d.) of Fe/Al through Units I to III as a function of water depth in the Black Sea.

bathed in sulfidic solutions (e.g., Raiswell and Berner, 1985; Boesen and Postma, 1988; Dean and Arthur, 1989; Middelburg, 1991; Lyons and Berner, 1992; Suits and Wilkin, 1998; Henneke et al., 1997). In these environments, the amount of syngenetic pyrite relative to diagenetic pyrite is related to the extent that reactive iron is effectively reduced to Fe^{2+} and sulfidized in the water column.

The amount of iron in pyrite relative to the total amount of iron, $Fe_{py}/\Sigma Fe$, is similar for all cores in Unit I (0.26 ± 0.08, $n = 15$), Unit II (0.26 ± 0.07, $n = 55$), and Unit IIIa (0.24 ± 0.05, $n = 18$). The fine-grained turbidites have similar Fe/Al ratios relative to Units I to III but lower $Fe_{py}/\Sigma Fe$ (0.21 ± 0.02). In the laminated sediments of Units I and II, DOP values tend to increase from the basin margins to the basin center (see Canfield et al., 1996; Lyons, 1997). In GC48, the amount of HCl-extractable Fe in Units I to III is 1.08 ± 0.10 wt.% (carbonate free) and is similar to the amount of extractable Fe in the turbiditic mud flows found in the deep basin sediments (1.03 ± 0.11, $n = 7$). On one hand these data could mean that the rate of pyritization increases with increasing water depth, or on the other hand, that proportionately less residual iron is deposited in the deep basin sediments. In this way DOP values reflect a reactive iron control on pyritization and also proximity to the basin margin. Evidence for subtle but significant changes in the composition of the Fe burial flux is shown for Units I to III in Figure 11, in which Fe/Al increases systematically and becomes more variable with greater depth. Only GC59 falls off the general trend, probably because this site resides on a mid-basin high and is expected to receive lower flux of particulate material derived from downslope or cross-shelf transport, i.e., the sediment chemistry at GC59 should match that in the deep basin. Accumulation rate data (Arthur and Dean, 1998) indicate that the fluxes of organic carbon and carbonate are similar from margin to basin center, but that clastic dilution is highest at the margins, hence the percentage of organic carbon and $CaCO_3$ increase systematically basinward. Thus, initial concentration of reactive iron and/or pyrite could be higher in more slowly deposited, deep basin sediments because of lower rates of clastic dilution in that region.

Two end-member models are possible to explain the history of pyrite formation in Unit III: (1) sulfur-limited pyrite formation throughout the deposition of Unit III followed by seawater

influx and consequent downward diffusion of H_2S/SO_4^{2-} at the Unit III–II boundary or (2) primary record where the Unit IIIb–IIIa boundary marks the incursion of sulfate-rich waters into the Black Sea, so that pyrite formation in Unit IIIa is not S-limited but rather is C-limited. Leventhal (1995) argued that, in general, pyrite sulfur-rich and organic carbon-poor sediments like those of unit IIIa are likely due to post-deposition sulfidation in response to changing water column salinity (see also Middelburg, 1991; Passier et al., 1996), i.e., model 1. The observed patterns in pyrite abundance, DOP values, and S-isotope trends are not exclusive to either model. Consistent with both of the above scenarios, pyrite formation in Unit IIIb appears to be limited by sulfur based on positive $\delta^{34}S$ values and low pyrite concentrations. The core logs indicate that in all cores, Unit IIIb contains crude banding of dark-colored layers that upon exposure to air oxidize to a mixture of rust-colored iron hydroxides and iron oxides. Unit IIIb is presumably the iron monosulfide-rich banded sediments described by Berner (1974). Following the above models, the persistence of iron monosulfides in Unit IIIb suggests an insufficient amount of oxidizing compounds (O_2 or S_x^{2-}) to convert iron monosulfides to pyrite. In anoxic, sulfate-depleted porewaters, any sulfide produced by in situ sulfate reduction or made available via diffusion from an overlying reservoir is rapidly sequestered by oxidation reactions with iron and manganese minerals; consequently, Fe^{2+}/HS^- ratios may remain high and effectively stabilize iron monosulfides over pyrite (see Eqn. 2).

Although the Unit II-III boundary surely marks the transition to bottom water anoxia in the Black Sea, it is possible that sulfate concentrations in the water column had begun to build up before this time (see Arthur and Dean, 1998). Sometime after the deposition of Unit IIIb, pyrite formation likely became limited, not by sulfate abundance, but rather by the reactivity of organic carbon. At that time, the abundance in Unit IIIa of pyrite and organic carbon would have likely clustered along normal marine trend as shown in Figure 8a. Movement off the normal marine trend toward the "euxinic" trend would have commenced after hydrogen sulfide concentrations had built up in the water column and had begun to diffuse downward into Unit IIIa. In Unit IIIa, a significant fraction of pyrite grains are uniquely non-framboidal and non-euhedral, both textures typical of sedimentary pyrite. Instead, many particles are coarse grained (<35 μm), non-equant masses (Fig. 3). This texture is unlike those formed near sedimentary redox transitions (Wilkin et al., 1996) and may be the result of iron oxyhydroxides (Unit IIIb) exposed to the diffusion of sulfide-rich solutions from above.

If the Unit II–III boundary represents a point when downward diffusion of ΣH_2S concomitant pyritization commenced, significant are the differences among the cores in the thickness of Unit IIIa. In the shallowest core, GC48, the thickness of Unit IIIa is ~55 cm. The maximum thickness of Unit IIIa (200 cm) is found in GC59 and is comparable to that of core BS4 to 14GC from 2218 m described by Calvert et al. (1996). Thus, the depth of the presumed diffusion front in GC48 is ~28% of that in the deeper cores. Berner (1969) developed a theoretical model for evaluating the kinetics of diffusion and reaction in hypothetical systems where sediments rich in organic carbon were deposited over organic carbon-poor sediments. In the situation where reactive iron is exhausted in the overlying organic carbon-rich sediment, the downward advance of the iron sulfide reaction front can be described by:

$$fL\,\frac{dX}{dt} = -\Phi D_s \left|\frac{\partial \Sigma H_2S}{\partial x}\right| x = X, \qquad (3)$$

where X = position of the sulfidation front below the Unit II–III boundary (cm), t = time (y), Φ = porosity, D_S = sediment diffusion coefficient of ΣH_2S (cm^2/yr), f = concentration of reactive iron in Unit III ($\mu mol/cm^3$), and L = number of moles of ΣH_2S consumed per mole of Fe reacted to form an iron sulfide. For the case where $X/2 \cdot (D_S \cdot t)^{1/2} < 0.7$, Eqn. 3 can be solved to give the position of the reaction front as a function of time with the expression:

$$X^2 = \frac{4\Phi[H_2S]^0\, D_s}{\sqrt{\pi} fL + \Phi[\Sigma H_2S]^0} \qquad (4)$$

For X = 55 cm, t = 7500 yr, and D_S = 270 cm^2/yr, $X/2 \cdot (D_S \cdot t)^{1/2} = 0.05$, so the equation should yield a reasonable solution (Berner, 1969). On the basis of Eqn. 4, the difference in thickness of Unit IIIa among the various cores can be evaluated. Assuming that in all cores, downward diffusion begins simultaneously and that the amounts of reactive iron and D_S are equivalent, the difference in the thickness of Unit IIIa in GC48 and GC59 can be explained by a ΣH_2S concentration in GC48 that is ~16% of that in the deep basin. In general, a lower time-integrated sulfide concentration in the water column over GC48 would lead to a shorter zone of diffusion. The previous assumption is reasonable in that laminated sediments of Unit II commence at the same effective radiocarbon date in all cores, including GC48 (e.g., Jones and Gagnon, 1994). Alternatively, the abundance of reactive iron could have been greater in either Unit II or III of GC48 as to retard the advance of the sulfide front. The difference between GC48 and GC59 makes sense when viewed in the context of their relative paleodepths. GC48 lies at a depth of 205 m below the sea surface near the depth of the chemocline. Various data (Huang et al., 2000) suggest that water column sulfate reduction above this site was intermittent, e.g., that oxic conditions may have prevailed at times at the sediment-water interface at the GC48 site as the result of downward excursions of the pycnocline/chemocline.

6. CONCLUSIONS AND IMPLICATIONS

Our studies highlight the utility of using textural properties of pyrite to: (1) distinguish anoxic vs. oxic depositional environments and (2) recognize both syngenetic and diagenetic components of pyritization in sediments deposited under anoxic and sulfidic water columns. More work is needed to evaluate whether these different textural components have unique isotopic signatures and, thereby, to provide information about the isotopic composition of ΣH_2S in ancient oceans and porewaters. These tools, then, should help in the interpretation of ancient sedimentary successions (e.g., Wilkin et al., 1996, 1997; Wignall and Newton, 1998), especially if narrow framboid size distributions correspond to laminated, organic carbon-rich shales. In this context, the addition of $\delta^{34}S$ values of pyrite help resolve depositional conditions, but sulfur isotope ratios do not simply correspond to water column redox chemistry. It

appears that the $\delta^{34}S$ of dissolved sulfide in the water column is controlled by other processes, such as the rate and relative amount of sulfide oxidation compared to sulfate reduction near the chemocline and, of course, the temporal change in $\delta^{34}S$ of oceanic sulfate reflecting changes in global S cycling.

Our model for the Black Sea indicates that fundamental controls on the amount of pyrite formed have changed over the past 15 ka, represented by approximately 400 cm, from sulfate-limited to carbon-limited, and finally, to Fe-limited as the system evolved from a freshwater lake to a brackish lake and then to the present stratified anoxic-sulfidic water column.

Acknowledgments—This research was supported by NSF grant EAR-9628344. We thank W. Dean for providing XRF data for cores GC59, 79, and 66 and for many discussions of aspects of Holocene Black Sea paleoenvironments, and we thank A. Owsley for assistance with the iron extractions, D. Walizer for help with isotope analyses, and Y. Huang for collecting core samples from the WHOI archives. Thoughtful reviews by M. Goldhaber, J. Middelburg, and T. Lyons helped improve the manuscript.

Associate editor: S. A. Wood

REFERENCES

Arthur M. A. and Sageman B. B. (1994) Marine black shales: Depositional mechanisms and environments of ancient deposits. *Ann. Rev. Earth Planet. Sci.* **22,** 499–551.

Arthur M. A., Dean W. E., Neff E. D., Hay B. J., King J., and Jones G. (1994) Varve calibrated records of carbonate over the last 2000 years in the Black Sea. *Global Biogeochem. Cycles* **8,** 195–217.

Arthur M. A. and Dean W. E. (1998) Organic-matter production and preservation and evolution of anoxia in the Holocene Black Sea. *Paleoceanography* **13,** 395–411.

Benning L. G., Wilkin R. T., and Barnes H. L. (2000) Reaction pathways in the Fe-S system below 100°C. *Chem. Geol.* **167,** 25–51.

Berner R. A. (1969) Migration of iron and sulfur within anaerobic sediments during early diagenesis. *Am. J. Sci.* **267,** 19–42.

Berner R. A. (1970) Sedimentary pyrite formation. *Am. J. Sci.* **268,** 1–23.

Berner R. A. (1974) Iron sulfides in Pleistocene deep Black Sea sediments and their paleo-oceanographic significance. In *Black Sea-Geology, Chemistry, and Biology* (eds. E. T. Degens and D. A. Ross), *Am. Assoc. Pet. Geol. Mem.* **20,** 524–531.

Berner R. A. (1984) Sedimentary pyrite formation: An update. *Geochim. Cosmochim. Acta* **48,** 605–615.

Boesen C. and Postma D. (1988) Pyrite formation in anoxic environments of the Baltic Sea. *Am. J. Sci.* **288,** 575–603.

Calvert S. E. (1990) Geochemistry and origin of the Holocene sapropel in the Black Sea. In *Facets of Modern Biogeochemistry* (eds. V. Ittekot, S. Kempe, W. Michaelis, and A. Spitzy), pp. 326–352. Springer-Verlag, New York.

Calvert S. E. and Karlin R. E. (1991) Relationships between sulphur, organic carbon, and iron in the modern sediments of the Black Sea. *Geochim. Cosmochim. Acta* **55,** 2483–2490.

Calvert S. E., Thode H. D., Yeung D., and Karlin R. E. (1996) A stable isotope study of pyrite formation in the Late Pleistocene and Holocene sediments of the Black Sea. *Geochim. Cosmochim. Acta* **60,** 1261–1270.

Canfield D. E., Raiswell R., Westrich J. T., Reaves C. M., and Berner R. A. (1986) The use of chromium reduction in the analysis of reduced inorganic sulfur in sediments and shales. *Chem. Geol.* **54,** 149–155.

Canfield D. E., Lyons T. W., and Raiswell R. (1996) A model for iron deposition to euxinic Black Sea sediments. *Am. J. Sci.* **296,** 818–834.

Canfield D. E, Thamdrup B., and Fleischer S. (1998) Isotope fractionation and sulphur metabolism by pure enrichment cultures of elemental sulfur-disproportionating bacteria. *Limnol. Oceanogr.* **43,** 253–264.

Dean W. E. and Arthur M. A. (1989) Iron-sulfur-carbon relationships in organic-carbon-rich sequences I: Cretaceous western interior seaway. *Am. J. Sci.* **289,** 708–743.

Degens E. T. and Ross D. A. (1972) Chronology of the Black Sea over the last 25,000 years. *Chem. Geol.* **10,** 1–16.

Degens E. T. and Stoffers P. (1976) Stratified waters as a key to the past. *Nature* **263,** 22–26.

Degens E. T., Michaelis W., Garrasi C., Mopper K., Kempe S., and Ittekkot A. (1980) Warven-chronologie und frühdiagenetische umsetzungen organischer substanzen holozaner sediments des Schwarzen Meeres. *Neues Jahrb. Geol. Palaeontol. Monatsh.* **83,** 65–86.

Deuser W. G. (1974) Evolution of anoxic conditions in Black Sea during Holocene. In *Black Sea-Geology, Chemistry, and Biology* (ed. E. T. Degens and D. A. Ross), *Am. Assoc. Pet. Geol. Mem.* **20,** 133–136.

dos Santos A. M. and Stumm W. (1992). Reductive dissolution of iron (III)(hydr)oxides by hydrogen sulfide. *Langmuir* **8,** 1671–1675.

Fry B., Jannasch H. W., Molyneaux S. J., Wirsen C. O., Muramoto J. A., and King S. (1991) Stable isotope studies of carbon, nitrogen and sulfur cycles in the Black Sea and the Cariaco trench. *Deep-Sea Res.* **38**(suppl. 2)**,** S1003–S1019.

Gagnon C., Mucci A., and Pelletier E. (1995) Anomalous accumulation of acid-volatile sulphides (AVS) in a coastal marine sediment. *Geochim. Cosmochim. Acta* **59,** 2663–2675.

Glenn C. R. and Arthur M. A. (1985) Sedimentary and geochemical indicators of productivity and oxygen contents in modern and ancient basins: The Holocene Black Sea as the "type" anoxic basin. *Chem. Geol.* **48,** 325–354.

Goldhaber M. B. and Kaplan I. R. (1974) The sulfur cycle. In *The Sea, Vol. 5, Marine Chemistry* (ed. E. D. Goldberg), pp. 569–655. Wiley.

Hay B. K., Arthur M. A., Dean W. E., Neff E. D., and Honjo S. (1991) Sediment deposition in the Late Holocene abyssal Black Sea with climatic and chronological implications. *Deep-Sea Res.* **38**(suppl. 2)**,** S1211–S1235.

Henneke E., Luther G. W. III, De Lange G. J., and Hoefs J. (1997) Sulphur speciation in anoxic hypersaline sediments from the eastern Mediterranean Sea. *Geochim. Cosmochim. Acta* **61,** 307–321.

Huang Y., Freeman K. H., Wilkin R. T., and Jones A. D. (2000) Black Sea chemocline oscillations during the Holocene: Molecular and isotopic studies of marginal sediments. *Org. Chem.* **31,** 1525–1531.

Hurtgen M. T., Lyons T. W., Ingall E. D., and Cruse A. M. (1999) Anomalous enrichments of iron monosulfide in euxinic marine sediments and the role of H_2S in iron sulfide transformations: Examples from Effingham Inlet, Orca Basin, and the Black Sea. *Am. J. Sci.* **299,** 556–588.

Jones G. A. and Gagnon A. R. (1994) Radiocarbon chronology of Black Sea sediments. *Deep-Sea Res.* **41,** 531–557.

Jørgensen B. B. (1990) A thiosulfate shunt in the sulfur cycle of marine sediments. *Science* **249,** 152–154.

Jørgensen B. B., Fossing H., Wirsen C. O., and Jannasch H. W. (1991) Sulfide oxidation in the anoxic Black Sea chemocline. *Deep-Sea Res.* **38**(suppl. 2)**,** S1083–S1103.

Kostka J. E. and Luther G. W. (1994) Partitioning and speciation of solid phase iron in salt marsh sediments. *Geochim. Cosmochim. Acta* **58,** 1701–1710.

Leventhal J. S. (1983) An interpretation of carbon and sulfur relationships in Black Sea sediments as indicators of environments of deposition. *Geochim. Cosmochim. Acta* **47,** 133–138.

Leventhal J. S. and Taylor C. (1990) Comparison of methods to determine degree of pyritization. *Geochim. Cosmochim. Acta* **54,** 2621–2625.

Leventhal J. S. (1995) Carbon-sulfur plots to show diagenetic and epigenetic sulfidation in sediments. *Geochim. Cosmchim. Acta* **59,** 1207–1211.

Limonov A. F., van Weering T. C. E., Kenyon N. H., Ivanov M. K., and Meisner L. B. (1997) Seabed morphology and gas venting in the Black Sea mudvolcano area: Observations with MAK-1 deep-tow sidescan sonar and bottom profiler. *Mar. Geol.* **137,** 121–136.

Love L. G. (1971) Early diagenetic polyframboidal pyrite, primary and redeposited, from the Wenlockian Denbigh Grit Group, Conway, North Wales, U.K. *J. Sed. Pet.* **41,** 1038–1044.

Love L. G. and Amstutz G. C. (1966) Review of microscopic pyrite

from the Devonian Chattanooga Shale and Rammelsberg Banderz. *Fortschr. Mineral.* **43,** 273–309.

Lyons T. W. (1991) Upper Holocene sediments of the Black Sea: Summary of Leg 4 box cores (1988 Black Sea Oceanographic Expedition). In *Black Sea Oceanography* (ed. E. Izdar and J. W. Murray), pp. 401–441. NATO ASI Series, Kluwer.

Lyons T. W. (1997) Sulfur isotopic trends and pathways of iron sulfide formation in upper Holocene sediments of the anoxic Black Sea. *Geochim. Cosmochim. Acta* **61,** 3367–3382.

Lyons T. W. and Berner R. A. (1992) Carbon-sulfur-iron systematics of the uppermost deep-water sediments of the Black Sea. *Chem. Geol.* **99,** 1–27.

Lyons T. W., Berner R. A., and Anderson R. F. (1993) Evidence for large pre-industrial perturbations of the Black Sea chemocline. *Nature* **365,** 538–540.

Middelburg J. J. (1991) Organic carbon, sulphur, and iron in recent semi-euxinic sediments of Kau Bay, Idonesia. *Geochim. Cosmochim. Acta* **55,** 815–828.

Millero F. J. (1991) The oxidation of H_2S in Black Sea waters. *Deep-Sea Res.* **38**(suppl. 2)**,** S1139–S1150.

Morse J. W. and Berner R. A. (1995) What controls sedimentary C/S ratios? *Geochim. Cosmochim. Acta* **59,** 1073–1077.

Muramoto J. A., Honjo S., Fry B., Howarth R. W., and Cisne J. L. (1991) Sulfur, iron and organic carbon fluxes in the Black Sea: Sulfur isotopic evidence for origin of sulfur fluxes. *Deep-Sea Res.* **38**(suppl. 2)**,** S1151–S1187.

Murray J. A., Jannasch H. W., Honjo S., Anderson R. F., Reeburgh W. S., Friederich G. E., Codispoti L. A., and Izdar E. (1989) Unexpected changes in the oxic/anoxic interface in the Black Sea. *Nature* **338,** 411–413.

Özsoy E. and Ünlüata U. (1997) Oceanography of the Black Sea: A review of some recent results. *Earth-Science Rev.* **42,** 231–272.

Passier H. F., Middelburg J. J., van Os B. J. H., and de Lange G. J. (1996). Diagenetic pyritisation under eastern Mediterranean sapropels caused by downward sulphide diffusion. *Geochim. Cosmochim. Acta* **60,** 751–763.

Passier H. F., Middelburg J. J., de Lange G. J., and Bottcher M. E. (1997) Pyrite contents, microtextures, and sulfur isotopes in relation to formation of the youngest eastern Mediterranean sapropel. *Geology* **25,** 519–522.

Pedersen T. F. and Calvert S. E. (1990) Anoxia vs. Productivity: What controls the formation of organic-carbon-rich sediments and sedimentary rocks. *Am. Assoc. Pet. Geol. Bull.* **74,** 454–466.

Pyzik A. J. and Sommer S. E. (1981) Sedimentary iron monosulfides: kinetics and mechanism of formation. *Geochim. Cosmochim. Acta* **45,** 687–698.

Raiswell R. (1982) Pyrite texture, isotopic composition and the availability of iron. *Am. J. Sci.* **82,** 1244–1263.

Raiswell R. and Berner R. A. (1985) Pyrite formation in euxinic and semi-euxinic sediments. *Am. J. Sci.* **285,** 710–724.

Raiswell R., Buckley F., Berner R. A., and Anderson T. F. (1988) Degree of pyritization of iron as a paleoenvironmental indicator of bottom-water oxygenation. *J. Sed. Pet.* **58,** 812–819.

Rickard D. T. (1974) Kinetics and mechanism of the sulfidation of goethite. *Am. J. Sci.* **274,** 941–952.

Rickard D. T. (1997) Kinetics of pyrite formation by the H_2S oxidation of iron(II) monosulfide in aqueous solutions between 25°C and 125°C: The rate equation. *Geochim. Cosmochim. Acta* **61,** 115–134.

Ross D. A. and Degens E. T. (1974) Recent sediments of the Black Sea. In *Black Sea-Geology, Chemistry, and Biology* (ed. E. T. Degens and D. A. Ross), *Am. Assoc. Pet. Geol. Mem.* **20,** 183–199.

Rozanov A. G., Volkov I. I., and Yagodinskaya T. A. (1974) Forms of iron in surface layer of Black Sea sediments. In *Black Sea-Geology, Chemistry, and Biology* (ed. E.T. Degens and D.A. Ross), *Am. Assoc. Pet. Geol. Mem.* **20,** 532–541.

Ryan W., Pitman W., Major C., Shimkus K., Moskalenko V., Jones G., Dimitrov P., Gorür N., Sakinç M., and Yüce H. (1997) An abrupt drowning of the Black Sea shelf. *Mar. Geol.* **138,** 119–126.

Sinninghe Damsté J. S., Wakeham S. G., Kohnen M. E. L., Hayes J., and de Leeuw J. W. (1993) A 6,000-year sedimentary molecular record of chemocline excursions in the Black Sea. *Nature* **362,** 827–829.

Suits N. S. and Wilkin R. T. (1998) Pyrite formation in the water column and sediments of a meromictic lake. *Geology* **26,** 1099–1102.

Sweeney R. E. and Kaplan I. R. (1980) Stable isotope composition of dissolved sulfate and hydrogen sulfide in the Black Sea. *Mar. Chem.* **9,** 145–152.

Vinogradov A. P., Grinenko V. A., and Ustinov V. I. (1962) Isotopic composition of sulphur compounds in the Black Sea. *Geokhim.* **7,** 973–997.

Wignall P. B. and Newton R. (1998) Pyrite framboid diameter as a measure of oxygen deficiency in ancient mudrocks. *Am. J. Sci.* **298,** 537–552.

Wilkin R. T., Barnes H. L., and Brantley S. L. (1996) The size distribution of framboidal pyrite in modern sediments: An indicator of redox conditions. *Geochim. Cosmochim. Acta* **60,** 3897–3912.

Wilkin R. T. and Barnes H. L. (1996) Pyrite formation by reactions of iron monosulfides with dissolved inorganic and organic sulfur species. *Geochim. Cosmochim. Acta* **60,** 4167–4179.

Wilkin R. T. and Barnes H. L. (1997a) Pyrite formation in an anoxic estuarine basin. *Am. J. Sci.* **297,** 620–650.

Wilkin R. T. and Barnes H. L. (1997b) Formation processes of framboidal pyrite. *Geochim. Cosmochim. Acta* **61,** 323–339.

Wilkin R. T., Arthur M. A., and Dean W. E. (1997) History of water-column anoxia in the Black Sea indicated by pyrite framboid size distributions. *Earth Planet. Sci. Lett.* **148,** 517–525.